

# Contact with coupled adhesion and friction: Computational framework, applications, and new insights

Janine C. Mergel<sup>1,2,a</sup>, Julien Scheibert<sup>b</sup>, Roger A. Sauer<sup>1,a,c</sup>

<sup>a</sup>*Graduate School AICES, RWTH Aachen University, Templergraben 55, 52056 Aachen, Germany*

<sup>b</sup>*Université de Lyon, Ecole Centrale de Lyon, ENISE, ENTPE, CNRS, Laboratoire de Tribologie et Dynamique des Systèmes LTDS, UMR 5513, F-69134, Ecully, France*

<sup>c</sup>*Department of Mechanical Engineering, Indian Institute of Technology Kanpur, UP 208016, India*

---

**Abstract:** Contact involving soft materials often combines dry adhesion, sliding friction, and large deformations. At the local level, these three aspects have been simultaneously captured only in the theoretical framework proposed by [Mergel et al. \(2019\)](#). We here develop a corresponding, nonlinear finite element framework that captures 3D finite-strain contact of two deformable bodies. This framework includes the two models by [Mergel et al. \(2019\)](#), and is suitable to investigate sliding friction even under tensile normal loads. First, we investigate our finite element model in test cases covering both 2D and 3D, ranging from compliant tapes to structures with high stiffness, and including deformable-rigid and deformable-deformable contact. We then provide new results on the onset of sliding of smooth elastomer-glass interfaces, which couples nonlinear material behavior, adhesion, and large frictional stresses. Our simulations not only agree well with both experimental and theoretical findings, they also provide new insights into the current debate on the shear-induced reduction of the contact area in elastomeric contact.

**Keywords:** dry adhesion, van der Waals interactions, sliding friction, nonlinear finite element methods, computational contact mechanics, elastomer contact

---

## 1 Introduction

Soft materials like compliant tapes, elastomers, and biological adhesive pads (appearing e.g. in insects and lizards) play a major role in a large variety of dry, solid contact. This kind of contact usually features large adhesive (or tensile) stresses, large frictional stresses, and large deformations, simultaneously. Present computational contact models do not account for all these three features at once. However, this would be desirable in order to reproduce and interpret a wide range of experimental observations for such systems, including gecko pads ([Autumn et al., 2002](#)), tape peeling ([De Zotti et al., 2019](#)), or rubber friction ([Sahli et al., 2018](#)).

For applications dominated by dry adhesion, the classical Coulomb-Amontons law of friction

$$F_t = \mu F_n, \quad F_n > 0, \quad (1)$$

relating the normal load  $F_n$  and the sliding friction force  $F_t$  by a coefficient of friction  $\mu$ , may not be valid anymore. For this reason, Eq. (1) was extended by an additional adhesion term ([Derjaguin, 1934](#)),

$$F_t = \mu F_n + \tau_0 A_{\text{real}} = \tau A_{\text{real}}, \quad \tau = \mu p_n + \tau_0. \quad (2)$$

---

<sup>1</sup>Corresponding authors, emails: janine.mergel@rwth-aachen.de, sauer@aices.rwth-aachen.de

<sup>2</sup>Former member of Graduate School AICES

Here, this will be referred to as the “extended” Amontons’ law of friction. In Eq. (2),  $A_{\text{real}}$  is the real area of contact (i.e., the total area of small microasperities in actual contact), and  $p_n = F_n/A_{\text{real}}$  is an averaged normal pressure. The term  $\tau_0$  denotes a critical shear stress that depends on both materials of the interacting surfaces. According to [Ruths et al. \(2005\)](#), Eq. (2) is suitable to describe the friction force between dry surfaces sliding over each other in the presence of adhesion. For large normal loads, the first term predominates (“pressure-controlled friction”), which again corresponds to the classical law of friction (1). If the normal pressure is small compared to the adhesive stresses, the second term predominates (“adhesion-controlled friction”). As shown experimentally by [Homola et al. \(1990\)](#) and others, it depends on the specific application which of these terms has stronger influence. The transition between both terms is also discussed in [Berman et al. \(1998\)](#), [Gao et al. \(2004\)](#), and [Jagota and Hui \(2011\)](#). Sometimes using a slightly different notation, relation (2) was considered in the context of microtribology ([Briscoe and Kremnitzer, 1979](#)), molecular dynamics ([Sivebæk et al., 2008](#); [Mo et al., 2009](#)), or adhesion and friction of biologic and bio-mimetic systems ([Zeng et al., 2009](#); [Hill et al., 2011](#)). It was further accounted for by [Tabor \(1981\)](#) to state a pressure-dependent, effective friction coefficient  $\hat{\mu} = \mu + \tau_0/p_n$ , which was then used e.g. in the friction model by [Wriggers et al. \(1990\)](#). Moreover, Eq. (2) is also known as Mohr-Coulomb criterion in soil mechanics.

Note that Eq. (2) refers to the total forces of a system as well as to the averaged normal pressure. Locally, however, the contact stresses may vary between tension and compression within the same macroscopic contact area (see e.g. measurements by [Eason et al. \(2015\)](#) for gecko toes). For this reason, [Mergel et al. \(2019\)](#) propose two general continuum contact models for dry adhesion and friction that are formulated in terms of local contact tractions:

- 1) Model DI: This model captures a constant (distance-independent) sliding resistance within the contact area, corresponding to purely adhesion-controlled friction.
- 2) Model EA: This model corresponds to a local version of extended Amontons’ law (2).

Up to a certain normal separation, both models are capable of capturing friction even for zero or negative (tensile) contact pressures. This approach is motivated by soft and compliant bio-adhesive pads, which are able to generate friction forces under tensile normal loads. Apart from the model derivation, [Mergel et al. \(2019\)](#) also provide a detailed literature review on the origin of adhesive friction<sup>3</sup> as well as new experimental results for an elastomer sphere sliding on a smooth glass plate. Besides, the above-mentioned paper contains a broad survey of existing models, proposed and applied in different disciplines. This overview captures e.g. cohesive zone models or approaches involving statistical homogenization, and also includes methods for both frictionless adhesion and non-adhesive friction. For a comprehensive review of models relevant to tribology, in general, see [Vakis et al. \(2018\)](#).

The first aim of the present paper is to formulate a computational framework for combined adhesion-friction models in general, and for the two above-mentioned models in particular. For the sake of self-consistency, here we briefly review our models from [Mergel et al. \(2019\)](#) as well as important assumptions. We then derive the equations that are necessary to implement these models into a nonlinear 3D finite element (FE) formulation based on large-deformation continuum mechanics. Such formulations go back to [Laursen and Simo \(1993\)](#), and were extended subsequently to consider e.g. thermomechanical contact ([Johansson and Klarbring, 1993](#)), wear ([Strömberg et al., 1996](#)), irreversible adhesion ([Raous et al., 1999](#)), reversible adhesion ([Sauer and Li, 2007a](#)), and multiscale contact ([Wriggers and Reinelt, 2009](#)). Note that the work of

---

<sup>3</sup>In the following, we use the term “adhesive friction” (instead of “frictional adhesion”) in order to emphasize that in our coupled models, friction depends on adhesion, and not vice versa.

Raous et al. (1999) contains separate models for adhesion and friction, and does not account for a dependency of friction on adhesion as is considered here. Regarding non-adhesive 3D frictional contact, important computational advancements were made in the context of surface smoothing (Padmanabhan and Laursen, 2001; Krstulović-Opara et al., 2002), mortar methods (Puso and Laursen, 2004; Gitterle et al., 2010; Dittmann et al., 2014), moving cone formulations (Wriggers and Krstulović-Opara, 2004), isogeometric analysis (De Lorenzis et al., 2011; Temizer et al., 2012), and unbiased friction algorithms (Sauer and De Lorenzis, 2015). The latter work is used as a basis for the present formulation.

The second aim of this paper is to provide various examples of application for our framework. The first three, although generic, especially serve to investigate the computational properties of our models. We then provide a detailed study of a fourth example, which is currently a matter of scientific debate in the literature: the onset of sliding of Hertz-like elastomer-glass contact. We here present new results that agree well with recent experimental (Sahli et al., 2019) and theoretical results (Chen et al., 2008; Papangelo et al., 2019). These results lead us to suggest that the shear-induced reduction of the contact area, discussed in those references, may exist even in the absence of adhesion.

The remainder of this paper is structured as follows. In Sect. 2 we state our general computational framework, and outline the two theoretical models that are motivated and derived in Mergel et al. (2019). Sect. 3 contains the algorithmic treatment of adhesive friction as well as the resulting finite element formulation. In Sect. 4 we address the validity of our models by discussing three applications in 2D and 3D, which range from soft and compliant tapes to rather stiff structures. A detailed study of the onset of sliding for smooth elastomer-glass contact follows in Sect. 5. Sect. 6 concludes this paper.

## 2 Continuum modeling of dry adhesion and friction

In order to describe adhesive friction between two bodies mathematically, we first define the separation of their surfaces. For this purpose we introduce a co-variant description for both surfaces, and define gap vectors along the normal and the tangential directions. As commonly done in continuum mechanics, we use uppercase letters for variables in the *reference* configuration of a body (denoted  $\mathcal{B}_0$ ), and small letters for variables in the *current* configuration ( $\mathcal{B}$ ).

### 2.1 Contact kinematics

For a certain material point on the contact surface of one body,  $\mathbf{x}_k \in \partial_c \mathcal{B}_k$  ( $k = 1, 2$ ), we need to determine its closest projection point,  $\mathbf{x}_p \in \partial_c \mathcal{B}_\ell$  ( $\ell = 2, 1$ ), that minimizes the distance between  $\mathbf{x}_k$  and the surface  $\partial_c \mathcal{B}_\ell$  of the neighboring body (Fig. 1). To this end, we assume that  $\partial_c \mathcal{B}_\ell$  can be parametrized by two convective coordinates  $\boldsymbol{\xi} = \{\xi^1, \xi^2\}$  such that  $\mathbf{x}_p = \mathbf{x}_\ell(\boldsymbol{\xi}_p)$ . At this (still unknown) point  $\mathbf{x}_p$ ,  $\partial_c \mathcal{B}_\ell$  is characterized by its co-variant and contra-variant tangent vectors,  $\mathbf{a}_\alpha^p$  and  $\mathbf{a}_p^\alpha$  ( $\alpha = 1, 2$ ), and by its surface normal  $\mathbf{n}_p$ . These vectors are defined as

$$\mathbf{a}_\alpha^p := \left. \frac{\partial \mathbf{x}_\ell(\boldsymbol{\xi})}{\partial \xi^\alpha} \right|_{\boldsymbol{\xi} = \boldsymbol{\xi}_p}, \quad (3)$$

$$\mathbf{a}_p^\alpha := a_p^{\alpha\beta} \mathbf{a}_\beta^p, \quad [a_p^{\alpha\beta}] = [a_{\alpha\beta}^p]^{-1}, \quad a_{\alpha\beta}^p = \mathbf{a}_\alpha^p \cdot \mathbf{a}_\beta^p, \quad (4)$$

$$\mathbf{n}_p := \frac{\mathbf{a}_1^p \times \mathbf{a}_2^p}{\|\mathbf{a}_1^p \times \mathbf{a}_2^p\|}, \quad (5)$$

where  $\times$  denotes the cross product, and the definition of  $\mathbf{a}_p^\alpha$  in Eq. (4) contains a summation over  $\beta = 1, 2$ . The coordinates  $\boldsymbol{\xi}_p$  of the projection point  $\mathbf{x}_p$  can then be determined by solving the (generally nonlinear) equations

$$(\mathbf{x}_p - \mathbf{x}_k) \cdot \mathbf{a}_\alpha^p = 0, \quad \alpha = 1, 2; \quad (6)$$

see e.g. Appx. B of [Sauer and De Lorenzis \(2015\)](#). Once this projection point is found, one can define a normal gap vector,  $\mathbf{g}_n$ , and a scalar normal gap,  $g_n$ , as

$$\mathbf{g}_n := \mathbf{x}_k - \mathbf{x}_p, \quad g_n := \mathbf{g}_n \cdot \mathbf{n}_p. \quad (7)$$

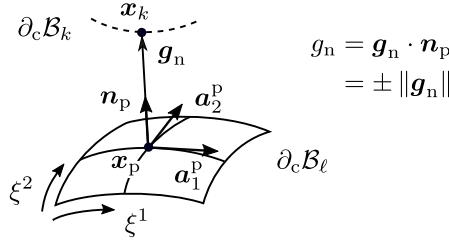


**Figure 1** Closest projection point,  $\mathbf{x}_p = \mathbf{x}_\ell(\boldsymbol{\xi}_p)$ , of  $\mathbf{x}_k$  onto surface  $\partial_c \mathcal{B}_\ell$ ; in the figure, the tangent vectors  $\mathbf{a}_\alpha^p$  ( $\alpha = 1, 2$ ), surface normal  $\mathbf{n}_p$ , and normal gap vector  $\mathbf{g}_n$  are illustrated.

In order to distinguish between tangential sticking and sliding, we (for now only conceptually) introduce a tangential slip vector,  $\mathbf{g}_t$ , which is decomposed into 1) a reversible (“elastic”) slip,  $\Delta \mathbf{g}_e$ , associated with sticking, and 2) an irreversible (“inelastic”) slip,  $\mathbf{g}_s$ , due to sliding,

$$\mathbf{g}_t = \mathbf{g}_s + \Delta \mathbf{g}_e. \quad (8)$$

This is used for the algorithmic treatment of friction in Sect. 3.1.

## 2.2 Modeling of adhesion and repulsion

For adhesive and repulsive contact between  $\mathcal{B}_k$  and  $\mathcal{B}_\ell$  we use the model of [Sauer and Li \(2007b\)](#) and [Sauer and Wriggers \(2009\)](#), which is based on an integrated Lennard-Jones potential. According to this model, the contact traction (force per area) at point  $\mathbf{x}_k \in \partial_c \mathcal{B}_k$ , due to  $\mathcal{B}_\ell$ , is given by

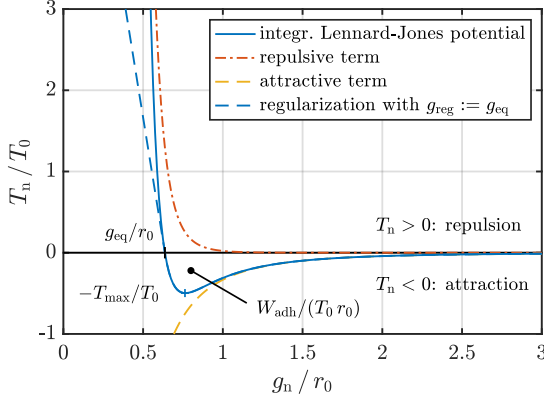
$$\mathbf{T}_{n,k} = \frac{\theta_k}{J_\ell} T_n(g_n) \mathbf{n}_p, \quad T_n(g_n) = \frac{A_H}{2\pi r_0^3} \left[ \frac{1}{45} \left( \frac{r_0}{g_n} \right)^9 - \frac{1}{3} \left( \frac{r_0}{g_n} \right)^3 \right]. \quad (9)$$

According to Eq. (9),  $\mathbf{T}_{n,k}$  depends on the normal vector and normal gap from Eqs. (5) and (7) as well as on the following quantities: the Hamaker constant  $A_H$ , the characteristic length  $r_0$  in the Lennard-Jones potential, the current volume change  $J_\ell$  around  $\mathbf{x}_p \in \partial_c \mathcal{B}_\ell$ , and a scalar  $\theta_k$  involving the inclination and deformation of the two bodies. In the following we use two assumptions discussed in full detail in [Mergel et al. \(2019\)](#):  $\theta_k \approx 1$  and  $J_\ell \approx J_{cl}$ , where  $J_{cl}$  is the local stretch of the surface  $\partial_c \mathcal{B}_\ell$ , given by

$$J_{cl} := \frac{j_{al}}{J_{Al}}, \quad j_{al} := \sqrt{\det [a_{\alpha\beta}^p]}, \quad J_{Al} := \sqrt{\det [A_{\alpha\beta}^p]}. \quad (10)$$

Here, the matrix entries of  $[a_{\alpha\beta}^p]$  and  $[A_{\alpha\beta}^p]$  ( $\alpha, \beta = 1, 2$ ) are determined from Eq. (4), inserting the co-variant tangent vectors from the current and the reference configurations,  $\mathbf{a}_\alpha^p$  and  $\mathbf{A}_\alpha^p = \partial \mathbf{X}_\ell(\boldsymbol{\xi}) / \partial \xi^\alpha|_{\boldsymbol{\xi}=\boldsymbol{\xi}_p}$ , respectively.

Note that the contact law of Eq. (9) is formulated with respect to the undeformed *reference* configuration; see also Mergel et al. (2019). Both the original model from Eq. (9) and its regularization addressed in Sauer (2011) and Mergel et al. (2019) are shown in Fig. 2, together with some additional, characteristic parameters.



#### Characteristic parameters:

- Equilibrium distance:  $g_{\text{eq}} = r_0 / \sqrt[6]{15}$
- Max. adhesive traction:  $T_{\text{max}} = \frac{\sqrt{5} A_H}{9\pi r_0^3}$
- Location of  $-T_{\text{max}}$ :  $g_{\text{max}} = r_0 / \sqrt[6]{5}$
- Work of adhesion:  $W_{\text{adh}} = \frac{\sqrt[3]{15} A_H}{16\pi r_0^2}$

**Figure 2** Normal contact traction in the model of Sauer and Wriggers (2009) for frictionless adhesion and repulsion as well as some characteristic parameters; here,  $T_0 = A_H / (2\pi r_0^3)$ , and the blue dashed line shows a regularization of  $T_n$  explained in Mergel et al. (2019).

## 2.3 General framework for sliding friction

We now discuss a general framework for combined adhesion, repulsion, and sliding friction. As specific examples we briefly outline two models from Mergel et al. (2019) as well as the relation of these models to the classical friction law by Coulomb and Amontons. The model equations stated in the remaining section as well as in the algorithm description (Sect. 3.1) all refer to friction between a surface point  $\mathbf{x}_\ell \in \partial_c \mathcal{B}_k$  and the neighboring surface  $\partial_c \mathcal{B}_\ell$ . For a shorter notation, we omit the indices  $k$  and  $\ell$  in the following.

In our framework we assume that the (vector-valued) tangential traction due to sticking and sliding friction depends on both the normal gap from Eq. (7) and the tangential slip vector introduced in Eq. (8), i.e.  $\mathbf{t}_t = \mathbf{t}_t(g_n, \mathbf{g}_t)$ . After defining a threshold function  $t_{\text{slide}}(g_n) \geq 0$  that limits the magnitude of the sliding traction  $\mathbf{t}_t$ , we consider friction laws of the general form

$$\|\mathbf{t}_t(g_n, \mathbf{g}_t)\| \begin{cases} < t_{\text{slide}}(g_n) & \text{during sticking,} \\ = t_{\text{slide}}(g_n) & \text{during sliding.} \end{cases} \quad (11)$$

In Eq. (11) we assume that, for equal  $g_n$ , the tangential traction required to initiate sliding (after sticking) is equal to the traction in the final sliding state. The motivation, validity, and restrictions of this assumption are addressed in detail in Mergel et al. (2019).

### 2.3.1 Classical law for Coulomb-Amontons friction

In the classical friction law by Coulomb and Amontons (stated for non-adhesive contact), the sliding threshold is given by the contact pressure multiplied with a coefficient of friction  $\mu$ ,

$$t_{\text{slide}}(g_n) = \mu t_n(g_n) \quad \text{if} \quad t_n(g_n) > 0. \quad (12)$$

### 2.3.2 Model DI: Distance-independent sliding friction in the contact area

For purely adhesion-controlled friction (e.g. for smooth contact surfaces and low normal pressures), the first theoretical model of [Mergel et al. \(2019\)](#) (DI) considers the sliding threshold to be constant at normal gap values smaller than a certain cutoff distance  $g_{\text{cut}}$ . This yields

$$t_{\text{slide}}(g_n) = \begin{cases} \tau_{\text{DI}}, & g_n \leq g_{\text{cut}}, \\ 0, & g_n > g_{\text{cut}}, \end{cases} \quad (13)$$

where  $\tau_{\text{DI}} > 0$  is a constant interface parameter. This model is motivated by various experimental results, e.g. by [Homola et al. \(1990\)](#), [Cohen et al. \(2011\)](#), [Sahli et al. \(2018\)](#) and [Mergel et al. \(2019\)](#). To overcome the discontinuity in Eq. (13) at  $g_n = g_{\text{cut}}$ , we further propose the following regularization,

$$t_{\text{slide}}(g_n) = \frac{\tau_{\text{DI}}}{1 + e^{k_{\text{DI}}(g_n - g_{\text{cut}})}}, \quad (14)$$

which will also be considered in our computational framework. Here,  $k_{\text{DI}} > 0$  is a sufficiently large regularization parameter for the transition between  $\tau_{\text{DI}}$  and zero. Both the unregularized and the regularized versions of model DI are shown in Fig. 3(a), together with the adhesion model from Sect. 2.2. Fig. 3(b) shows the resulting friction law, i.e., the traction-separation law in tangential direction for arbitrary but fixed normal distances. In contrast to the classical friction law (12), the sliding traction of model DI is independent from the normal traction. For comparison, we introduce a friction parameter<sup>4</sup>  $\mu_{\text{DI}} := \tau_{\text{DI}} / T_{\text{max}}$ , which relates the sliding traction to the maximum adhesive traction from Fig. 2.

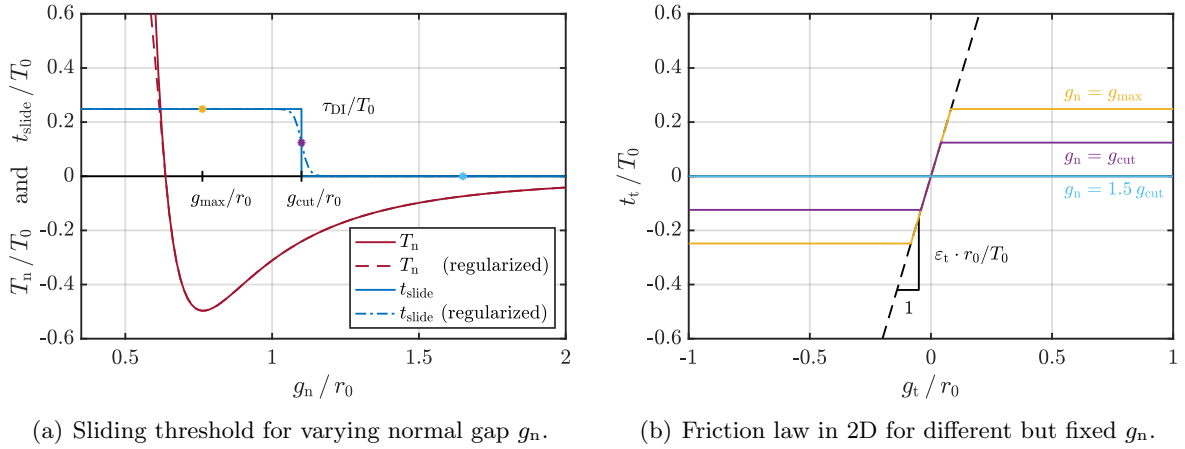


**Figure 3** Model DI: Constant sliding traction within the cutoff distance  $g_{\text{cut}}$  for  $\tau_{\text{DI}} = 0.5 T_{\text{max}}$ ,  $g_{\text{cut}} = 1.1 r_0$ , and  $k_{\text{DI}} = 80/r_0$ ; here,  $T_0 = A_H / (2\pi r_0^3)$ ; for  $\varepsilon_t$  see Sect. 3.1; the asterisks mark the distances  $g_{\text{max}}$  (where  $|T_n| = T_{\text{max}}$ , yellow),  $g_{\text{cut}}$  (purple) and  $1.5 g_{\text{cut}}$  (light blue).

Note that the adhesive-friction model DI is stated in the *current* configuration of the bodies, which means that the sliding threshold  $\tau_{\text{DI}}$  refers to the *actual* area of the contact interface. This point is discussed further in [Mergel \(2017\)](#) and [Mergel et al. \(2019\)](#). In these publications, also a list of related approaches (such as the model of [Deng et al. \(2012\)](#)) can be found.

<sup>4</sup>To avoid any confusion with the classical coefficient of friction  $\mu$  from Eq. (12) (i.e., the ratio between the frictional traction and the pressure), for our two models we use the terminology “friction parameter” instead.

### 2.3.3 Model EA: Extended Amontons' law in local form

The second adhesive-friction law in [Mergel et al. \(2019\)](#) is inspired by the classical Coulomb-Amontons law from Sect. 2.3.1 extended by an adhesion term. See that paper for the motivation and derivation of this model, including also a detailed review of related approaches.

According to model EA, the sliding threshold is proportional to the (shifted) normal traction from the adhesion model in Eq. (9). Let us first choose a normal distance somewhere between the equilibrium distance  $g_{\text{eq}}$  and the location  $g_{\text{max}}$  of  $-T_{\text{max}}$  (see Fig. 2):

$$g_{\text{cut}} = s_{\text{cut}} g_{\text{max}} + (1 - s_{\text{cut}}) g_{\text{eq}}, \quad s_{\text{cut}} \in [0, 1]. \quad (15)$$

As shown in Fig. 2, at  $g_{\text{cut}}$  the function value  $T_{\text{n}}(g_{\text{cut}})$  is either zero or negative. We then consider a sliding threshold that is proportional to the shifted curve  $T_{\text{n}}(g_{\text{n}}) + |T_{\text{n}}(g_{\text{cut}})|$ :

$$T_{\text{slide}}(g_{\text{n}}) = \begin{cases} \frac{\mu_{\text{EA}}}{J_{\text{cl}}} [T_{\text{n}}(g_{\text{n}}) - T_{\text{n}}(g_{\text{cut}})], & g_{\text{n}} < g_{\text{cut}}, \\ 0, & g_{\text{n}} \geq g_{\text{cut}}. \end{cases} \quad (16)$$

The scalar  $\mu_{\text{EA}} > 0$  denotes the friction parameter for model EA (see also footnote 4). Note that in this model, the sliding threshold directly depends on the normal traction, which is defined in the *reference* configuration.

Fig. 4 illustrates model EA for the parameter values  $s_{\text{cut}} = 0, 0.5$ , and 1. The left-hand side of the figure depicts the relation between the normal gap,  $g_{\text{n}}$ , and the sliding threshold,  $T_{\text{slide}}$ . Dashed lines indicate a regularization for small normal gaps discussed in the appendix of [Mergel et al. \(2019\)](#) and Sect. 3.4.2. In analogy to Fig. 3(b), the right-hand side of Fig. 4 shows the resulting friction laws.

For  $s_{\text{cut}} = 0$ , model EA provides a frictional resistance (i.e.,  $T_{\text{slide}} > 0$ ) only for positive, and thus compressive, normal tractions. This corresponds to the classical Coulomb-Amontons law for non-adhesive contact (but here stated in the initial configuration, cf. Eq. (12)). In a similar manner, sliding friction is included in various cohesive zone models ([Chaboche et al., 1997](#); [Raous et al., 1999](#); [Del Piero and Raous, 2010](#)). For  $s_{\text{cut}} > 0$ , the model provides (to some extent) a tangential sliding resistance even under tensile normal tractions. Note that the function  $T_{\text{slide}}(g_{\text{n}})$  is  $C^1$ -continuous only if  $s_{\text{cut}} = 1$  (Fig. 4(e)). In any other case, a kink occurs at  $g_{\text{n}} = g_{\text{cut}}$ , which requires a special algorithmic treatment in the solution strategy (Sect. 3.3).

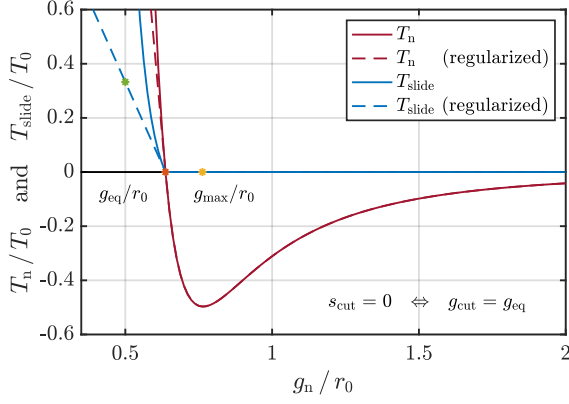
## 3 Computational framework

This section contains the algorithmic treatment of adhesive friction and details on its implementation into a nonlinear finite element code. We also address the validity and restrictions of our models.

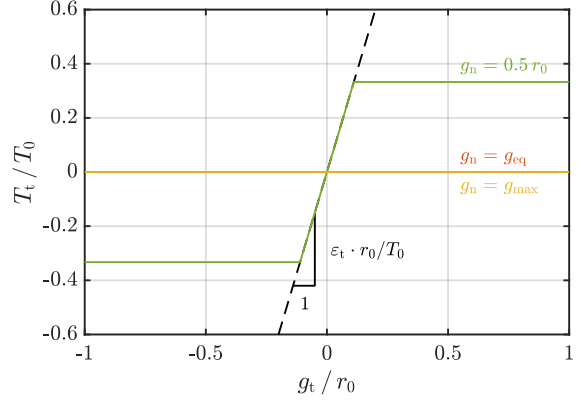
### 3.1 Algorithmic treatment of adhesive friction

In computational friction algorithms, sticking and sliding are often realized by means of a predictor-corrector approach similar to that used for elastoplasticity, see, e.g., [Simo and Hughes \(1998\)](#): One first predicts tangential sticking, checks whether the criterion for sliding is satisfied, and if so, applies a return map to determine the sliding distance.

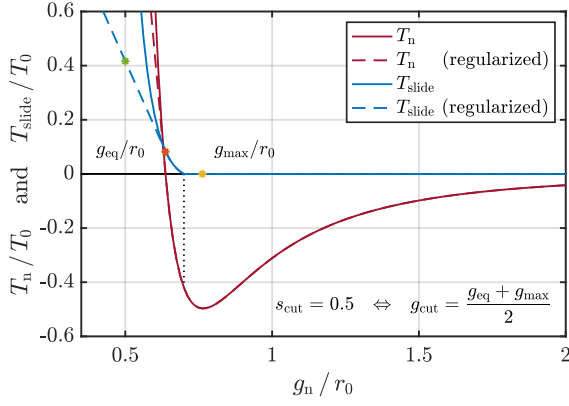




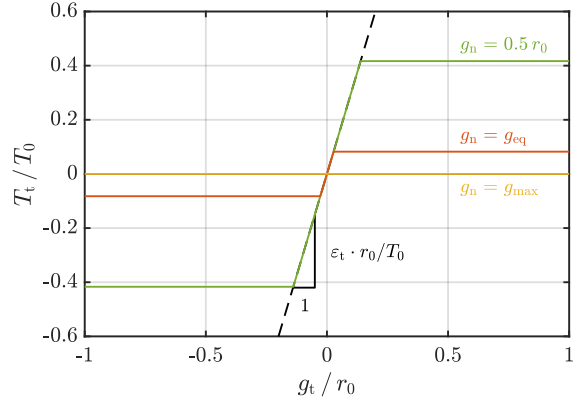
(a) Sliding threshold for varying  $g_n$ ;  $s_{\text{cut}} = 0$ .



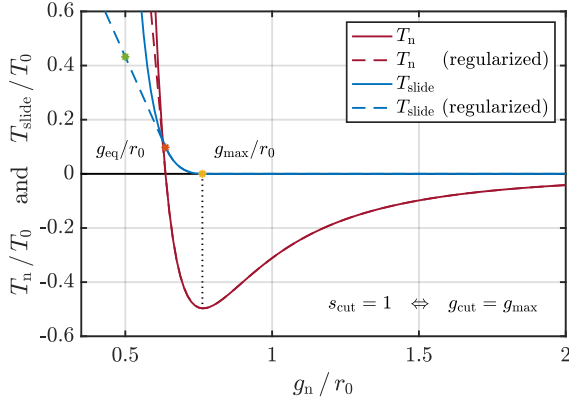
(b) 2D friction law for different but fixed  $g_n$ ;  $s_{\text{cut}} = 0$ .



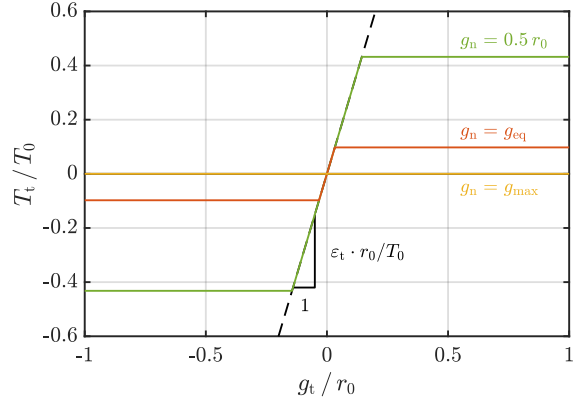
(c) Sliding threshold for varying  $g_n$ ;  $s_{\text{cut}} = 0.5$ .



(d) 2D friction law for different but fixed  $g_n$ ;  $s_{\text{cut}} = 0.5$ .



(e) Sliding threshold for varying  $g_n$ ;  $s_{\text{cut}} = 1$ .



(f) 2D friction law for different but fixed  $g_n$ ;  $s_{\text{cut}} = 1$ .

**Figure 4** Model EA: Extended Amontons' law in *local* form illustrated for  $\mu_{\text{EA}} = 0.2$ ,  $J_{\text{cl}} \equiv 1$ , and three different values of  $s_{\text{cut}}$ ; here,  $T_0 = A_{\text{H}}/(2\pi r_0^3)$ ; for  $\varepsilon_t$  see Sect. 3.1; the colored asterisks mark the distances  $0.5 r_0$  (green),  $g_{\text{eq}}$  (where  $T_n = 0$ , orange), and  $g_{\text{max}}$  (yellow).



The following algorithm is formulated in the current configuration, i.e., in terms of the variables  $\mathbf{t}_t$  and  $t_{\text{slide}}$ . Since model EA is formulated with respect to  $T_t$  and  $T_{\text{slide}}$  in the initial configuration (see Sect. 2.3.3), it is also possible to state the algorithm with respect to  $T_t$  and  $T_{\text{slide}}$ , as shown in Mergel (2017).

Let us start with a sliding criterion  $f_s \leq 0$  that satisfies (Wriggers, 2006)

$$f_s \begin{cases} < 0 & \text{for sticking,} \\ = 0 & \text{for sliding.} \end{cases} \quad (17)$$

In our case we define

$$f_s(\mathbf{t}_t, t_{\text{slide}}) := \|\mathbf{t}_t\| - t_{\text{slide}}. \quad (18)$$

During sliding we must enforce  $f_s(\mathbf{t}_t, t_{\text{slide}}) = 0$ , and determine both the direction and the magnitude of the resulting tangential gap. Since this projection step is carried out at a certain (pseudo-)time step, the normal gap from Eq. (7),  $g_n$ , is considered to be arbitrary but fixed. Note that for the models from Sects. 2.3.1 to 2.3.3, the domain of feasible tractions

$$\mathbb{E}_t := \left\{ \mathbf{t}_t \in \mathbb{R}^d \mid f_s(\mathbf{t}_t, t_{\text{slide}}) \leq 0 \right\} \quad (19)$$

is convex for arbitrary (but fixed)  $g_n$ , and  $f_s$  is convex in  $\mathbb{E}_t$  (Mergel, 2017). These properties ensure that the mapping performed as a corrective step will be unique. Let us now define the non-negative dissipation during sliding,

$$\mathcal{D}_s(\mathbf{t}_t; \mathcal{L}\mathbf{g}_s) := \mathbf{t}_t \cdot \mathcal{L}\mathbf{g}_s, \quad (20)$$

which represents the energy loss per time and area. The term

$$\mathcal{L}\mathbf{g}_s := \dot{\xi}_s^\alpha \mathbf{a}_\alpha^s, \quad \mathbf{a}_\alpha^s := \left. \frac{\partial \mathbf{x}_\ell(\boldsymbol{\xi})}{\partial \xi^\alpha} \right|_{\boldsymbol{\xi} = \boldsymbol{\xi}_s}, \quad (21)$$

denotes the relative inelastic slip velocity, i.e., the Lie derivative of the inelastic slip vector  $\mathbf{g}_s$  conceptually introduced in Eq. (8); see also Sauer and De Lorenzis (2015). Note that the dot denotes the material time derivative of  $\xi_s^\alpha$  (keeping material point  $\mathbf{X}_p$  fixed). According to the so-called principle of maximum dissipation (Simo and Hughes, 1998; Wriggers, 2006), for a *given* inelastic slip velocity  $\mathcal{L}\mathbf{g}_s$ , the actual (physically true) traction  $\mathbf{t}_t$  maximizes the dissipation among all feasible tractions  $\mathbf{t}_t^* \in \mathbb{E}_t$ . By keeping  $\mathcal{L}\mathbf{g}_s$  arbitrary but fixed, and by introducing the Lagrange multiplier  $\gamma \geq 0$ , we can then formulate the following constrained minimization problem

$$\left. \frac{\partial \mathcal{L}(\mathbf{t}_t^*, \gamma; \mathcal{L}\mathbf{g}_s)}{\partial \mathbf{t}_t^*} \right|_{\mathbf{t}_t^* = \mathbf{t}_t} = \mathbf{0} \quad (22)$$

with Lagrangian

$$\mathcal{L}(\mathbf{t}_t^*, \gamma; \mathcal{L}\mathbf{g}_s) := -\mathcal{D}_s(\mathbf{t}_t^*; \mathcal{L}\mathbf{g}_s) + \gamma \cdot f_s(\mathbf{t}_t^*, t_{\text{slide}}), \quad (23)$$

and the Karush-Kuhn-Tucker (KKT) conditions for optimality,

$$f_s \leq 0, \quad \gamma \geq 0, \quad f_s \cdot \gamma = 0. \quad (24)$$

From Eq. (22) we then obtain the evolution law for the slip velocity during sliding

$$\mathcal{L}\mathbf{g}_s = \gamma \mathbf{n}_t, \quad \mathbf{n}_t := \frac{\partial f_s}{\partial \mathbf{t}_t} = \frac{\mathbf{t}_t}{\|\mathbf{t}_t\|}. \quad (25)$$

According to Eq. (25), the multiplier  $\gamma$  corresponds to the magnitude of the tangential slip velocity. Since during sliding  $f_s = 0$ , the traction satisfies

$$\mathbf{t}_t = t_{\text{slide}} \mathbf{n}_t \quad (26)$$

as required. The time derivatives  $\dot{\xi}_s^\alpha$  in  $\mathcal{L}\mathbf{g}_s$  can finally be determined by inserting Eq. (25) into Eq. (21), and contracting the result with the tangent vectors  $\mathbf{a}_s^\alpha$ , giving

$$\dot{\xi}_s^\alpha = \gamma \mathbf{n}_t \cdot \mathbf{a}_s^\alpha, \quad \alpha = 1, 2. \quad (27)$$

The following procedure corresponds to the friction algorithm proposed by [Sauer and De Lorenzis \(2015\)](#), but extended to a general sliding threshold  $t_{\text{slide}}$ . For the derivation of the resulting equations we refer to the above-mentioned paper. The key idea is to decompose the convective coordinates,  $\xi_p^\alpha$ , of the projection point into components that are either related to irreversible sliding,  $\xi_s^\alpha$ , or to reversible (elastic) sticking,  $\Delta\xi_e^\alpha$  (cf. Eq. (8)).

Given all quantities at a pseudo-time step  $t_n$ , one proceeds to the next step  $t_{n+1}$  as follows:

- 
- 1) Assume tangential sticking and compute a corresponding elastic trial traction

$$\mathbf{t}_{\text{trial}}^{n+1} = \varepsilon_t [\mathbf{x}_\ell^{n+1}(\boldsymbol{\xi}_p^{n+1}) - \mathbf{x}_\ell^{n+1}(\boldsymbol{\xi}_s^n)]. \quad (28)$$

The penalty parameter  $\varepsilon_t$  is used for regularization, i.e., to allow for a small, reversible tangential gap.  $\varepsilon_t$  is visualized in Fig. 3(b) for model DI, and e.g. in Fig. 4(d) for model EA.

- 2) Insert  $\mathbf{t}_{\text{trial}}^{n+1}$  into the criterion

$$f_s(\mathbf{t}_{\text{trial}}^{n+1}, t_{\text{slide}}^{n+1}) = \|\mathbf{t}_{\text{trial}}^{n+1}\| - t_{\text{slide}}^{n+1}. \quad (29)$$

to check for sticking or sliding:

- (a) If  $f_s(\mathbf{t}_{\text{trial}}^{n+1}, t_{\text{slide}}^{n+1}) < 0$ , the point  $\mathbf{x}_p$  is sticking tangentially; thus

$$\mathbf{t}_t^{n+1} = \mathbf{t}_{\text{trial}}^{n+1}, \quad \xi_{s\,n+1}^\alpha = \xi_{s\,n}^\alpha, \quad \alpha = 1, 2. \quad (30)$$

- (b) If  $f_s(\mathbf{t}_{\text{trial}}^{n+1}, t_{\text{slide}}^{n+1}) \geq 0$ , the point  $\mathbf{x}_p$  is sliding; an additional correction is required to determine the actual traction  $\mathbf{t}_t^{n+1}$  such that it satisfies  $f_s(\mathbf{t}_t^{n+1}, t_{\text{slide}}^{n+1}) = 0$ . For this purpose one first computes the incremental update of the Lagrange multiplier in Eq. (25),

$$\Delta\gamma_{n+1} = \frac{f_s(\mathbf{t}_{\text{trial}}^{n+1}, t_{\text{slide}}^{n+1})}{\varepsilon_t}, \quad (31)$$

and then determines the slid distance as well as the vector of the tangential traction,

$$\xi_{s\,n+1}^\alpha = \xi_{s\,n}^\alpha + \Delta\gamma_{n+1} \mathbf{n}_t^{n+1} \cdot \mathbf{a}_{p\,n+1}^\alpha, \quad \mathbf{n}_t^{n+1} = \frac{\mathbf{t}_{\text{trial}}^{n+1}}{\|\mathbf{t}_{\text{trial}}^{n+1}\|}, \quad (32)$$

$$\mathbf{t}_t^{n+1} = \mathbf{t}_{\text{trial}}^{n+1} - \varepsilon_t \Delta\gamma_{n+1} \mathbf{n}_t^{n+1}. \quad (33)$$

Eq. (32) is based on the approximation  $\mathbf{a}_{p\,n+1}^\alpha \approx \mathbf{a}_{s\,n+1}^\alpha$  (see [Sauer and De Lorenzis \(2015\)](#)), and on the discretization of Eq. (27) by means of the implicit Euler method.

---

The traction  $\mathbf{t}_t^{n+1}$  in Eq. (33) satisfies Eq. (26). In the case of frictionless sliding (i.e.,  $t_{\text{slide}}^{n+1} = 0$ ), one simply sets  $\mathbf{t}_t^{n+1} = \mathbf{0}$  and  $\xi_{s\,n+1}^\alpha = \xi_{p\,n+1}^\alpha$ . Fig. 5 illustrates the return map performed during sliding for both models DI and EA. The colored surfaces in this figure correspond to the sliding thresholds  $t_{\text{slide}}$  and  $T_{\text{slide}}$  from Figs. 3(a) and 4(e), but revolved around the  $g_n$ -axis.

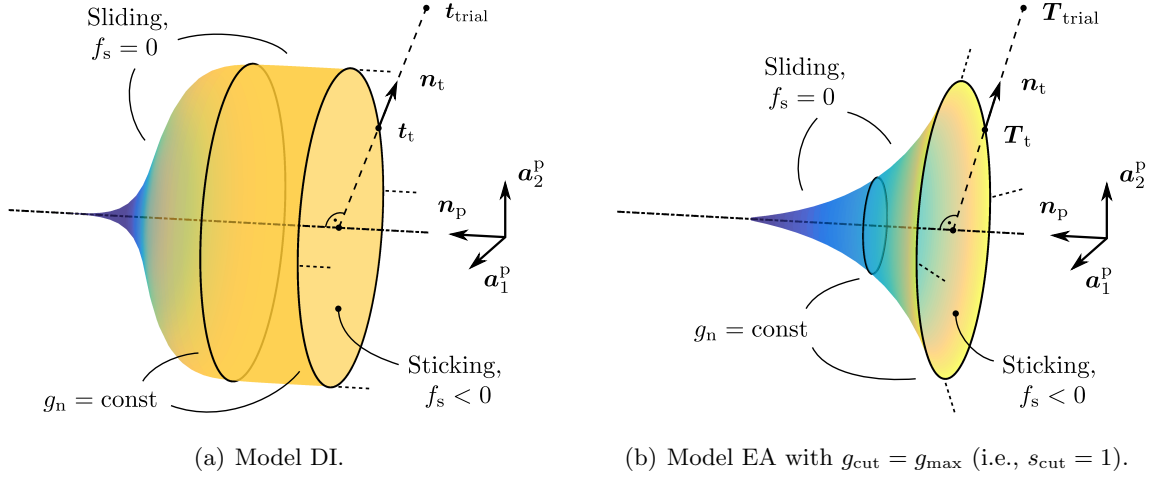


**Figure 5** Illustration of the return map performed in the corrector step for tangential sliding.

### 3.2 Contact contributions to the finite element equations

In order to discretize the corresponding model equations in space, we use a standard Galerkin finite element (FE) method. For the sake of brevity we only discuss the contact contributions here. To this end, we introduce a global FE contact force vector  $\mathbf{f}_c(\mathbf{u})$ , which depends on the global displacement vector  $\mathbf{u}$  for all finite element nodes. Following the sign convention by Laursen (2002), we now decompose  $\mathbf{f}_c(\mathbf{u})$  into the normal force  $\mathbf{f}_n$  due to adhesion and repulsion and the tangential force  $\mathbf{f}_t$  due to friction,

$$\mathbf{f}_c(\mathbf{u}) := \mathbf{f}_n(\mathbf{u}) - \mathbf{f}_t(\mathbf{u}). \quad (34)$$

$\mathbf{f}_n$  and  $\mathbf{f}_t$  are obtained by assembling the contributions from each finite element on the contact surfaces. For contact between two deformable bodies, we consider the *two-half-pass* approach by Sauer and De Lorenzis (2013, 2015). We thus iterate over the elements of *both* contact surfaces ( $k = 1, 2$ ), and compute the elemental contribution to the normal forces from

$$\mathbf{f}_{n,k}^e = - \int_{\Gamma_{c0k}^e} \mathbf{N}_k^T \mathbf{T}_{n,k} \, dA_k. \quad (35)$$

Here,  $\Gamma_{c0k}^e \subset \partial_c \mathcal{B}_{0k}^h$ ,  $\mathbf{T}_{n,k}$  is given by Eq. (9), and the array  $\mathbf{N}_k$  contains the nodal shape functions associated with the current element. The tangential forces are determined similarly,

$$\mathbf{f}_{t,k}^e = - \int_{\Gamma_{ck}^e} \mathbf{N}_k^T \mathbf{t}_{t,k} \, da_k = - \int_{\Gamma_{c0k}^e} \mathbf{N}_k^T \mathbf{T}_{t,k} \, dA_k, \quad (36)$$

depending on whether the model is defined in the current (model DI, Eq. (14)) or the reference configuration (model EA, Eq. (16)).

Since the vector  $\mathbf{f}_c$  is nonlinear with respect to  $\mathbf{u}$ , we linearize it to solve the governing equations with Newton's method. To this end, we derive the tangent matrix associated with  $\mathbf{f}_c$ , denoted  $\mathbf{k}_c := \partial \mathbf{f}_c / \partial \mathbf{u}$ . Like the global contact forces  $\mathbf{f}_n$  and  $\mathbf{f}_t$ ,  $\mathbf{k}_c$  is assembled from the contributions of each single surface element, see App. A. Finally, we evaluate the integrals in Eqs. (35) and (36) and App. A by means of Gaussian quadrature.

### 3.3 Active set strategy

As seen in Figs. 4(a) and 4(c), the curve  $T_{\text{slide}}(g_n)$  of model EA is  $C^1$ -continuous at the cutoff distance  $g_{\text{cut}}$  only if  $g_{\text{cut}} = g_{\text{max}}$  (i.e.,  $s_{\text{cut}} = 1$ ). Otherwise, it is  $C^0$ -continuous at  $g_{\text{cut}}$ . Moreover, we must generally distinguish between discrete states of contact like tangential sticking and sliding. Following Sauer and De Lorenzis (2015), we here consider an active set strategy. To this end, we slightly modify the two active sets that are often used for unilateral and frictional contact: (i) “(compressive) contact vs. no contact” and (ii) “sticking vs. sliding”. Since the function  $T_n(g_n)$  in Eq. (9) is continuous anyway (and thus does not require any active set at all), we simply replace active set (i) by “frictional vs. frictionless sliding”. Note that it is also reasonable to define certain cutoff values for which both the normal and tangential contact stresses are considered to be negligible. This increases the efficiency on one hand, and circumvents computational problems in the sliding algorithm or closest point projection (due to large separations of the bodies) on the other hand.

For changes in the (discrete) contact states, the FE force vector  $\mathbf{f}_c(\mathbf{u})$  actually becomes non-differentiable, cf. Apps. A.2.1 and A.2.2. If the applied load step is too large, or if large parts of the contact surface change their state at once, this may lead to a phenomenon called cycling, or also zig-zagging (Wriggers, 2006). That is, the solution algorithm alternates between two states in consecutive iterations. This can be overcome e.g. by means of semi-smooth Newton methods. We here pursue a strategy that is based on a temporary “freezing” of the active sets; see also Wriggers (2006). Accordingly, we keep the active sets fixed at the beginning of the iterations, until the residual falls below a certain tolerance. We then assume that the changes in the state are sufficiently small to prevent cycling. Further improvement can be made by adjusting the load step adaptively when the body starts or stops (full) sliding, in particular when it changes its direction of sliding.

A special case that should be treated with additional care is model EA with  $s_{\text{cut}} = 0$  (i.e.,  $g_{\text{cut}} = g_{\text{eq}}$ ), which is related to the classical Coulomb-Amontons law of (non-adhesive) friction (Sect. 2.3.1). For this specific case, the switch from frictional resistance to zero frictional resistance is directly located at the equilibrium distance,  $g_{\text{eq}}$ , where the normal traction is zero (Fig. 4(a)). Depending also on the problem setup, the tangential traction can then alternate back and forth between the states of frictional and frictionless sliding, either requiring unnecessarily small load steps or even leading to a failure of the freezing strategy. As demonstrated in Sect. 4.1, however, this issue can be successfully overcome by choosing a cutoff distance  $g_{\text{cut}}$  that is slightly *smaller* than  $g_{\text{eq}}$ . One hence considers Eq. (15) with a parameter  $s_{\text{cut}}$  that is negative but close to zero (e.g.,  $s_{\text{cut}} = -0.001$ ). Thus, the contact pressure must first exceed a certain threshold to generate a frictional resistance.

### 3.4 Validity, restrictions, and possible extensions of our models

Let us now discuss the validity and restrictions of our models, in particular regarding computational aspects. For physical assumptions we refer to Mergel et al. (2019). For the properties of the two-half-pass algorithm applied here (including advantages and disadvantages) see the original papers by Sauer and De Lorenzis (2013, 2015) and Mergel (2017). A possible extension of our models to incorporate sticking friction larger than the sliding resistance  $t_{\text{slide}}$  or  $T_{\text{slide}}$  is briefly addressed in Mergel (2017).

### 3.4.1 Jump-off and jump-to contact

Strong adhesion combined with soft materials may cause sudden jump-off or jump-to contact, see e.g. [Chaboche et al. \(2001\)](#) and [Sauer \(2006\)](#). In that case the (de-)bonding process inherently becomes unstable, and the governing equations do not necessarily have a unique solution when assuming quasi-static behavior. According to [Raous \(2011\)](#), this is caused by the non-convexity and the “softening character” (i.e., a decreasing slope with increasing distance) of traction-separation laws like the one in [Fig. 2](#). A similar effect can occur also for sliding friction ([Martins and Raous, 2002](#); [Mróz, 2002](#)). The issues mentioned above can be overcome by applying e.g. an arc length or continuation method for the solution of the model equations ([Sauer, 2006](#)). Another possibility is to account for a viscous regularization as done in several cohesive zone models involving friction ([Raous et al., 1999](#); [Chaboche et al., 2001](#); [Del Piero and Raous, 2010](#)). This approach is reasonable because viscous effects often occur not only in the bulk material but also at the interface. Besides, it is also possible to account for inertial effects and to consider the problem to be dynamic. Since the study of dynamic and viscous effects lies outside the scope of this paper, in our examples we focus on the attachment or detachment process itself, but not on sudden jump-to or jump-off contact, respectively.

### 3.4.2 Going from the nano- to the macroscale

As shown in [Fig. 2](#), the normal contact traction  $T_n$  decays rapidly for increasing distances  $g_n$ : Depending on the involved materials,  $T_n$  typically ranges only over several (tens of) nanometers. In addition, if  $g_n$  approaches zero, the traction increases to infinity while its slope approaches minus infinity. These issues can cause numerical problems on one hand, and require a fine spatial resolution (finite element size and applied displacements) on the other hand.

For scales up to hundreds or thousands of nanometers, these problems can be overcome with different strategies. First, a sufficiently accurate surface discretization is crucial to reduce artificial oscillations ([Sauer, 2011](#); [Corbett and Sauer, 2014](#)) that could cause difficulties in the convergence of the numerical solution procedure. In our numerical examples we thus use special, surface-enriched finite elements based either on Hermite ([Sauer, 2011](#)) or Non-Uniform Rational B-Spline (NURBS) shape functions ([Corbett and Sauer, 2014, 2015](#)). Second, we regularize our contact models for small normal gaps, as illustrated for normal contact in [Fig. 2](#), and for tangential contact in [Fig. 3\(a\)](#) and [Fig. 4](#) left. Third, we calibrate the model parameters from [Sect. 2.2](#) ( $A_H$ ,  $T_{\max}$ , and  $W_{\text{adh}}$ ) such that they match experimental data. This leads to a larger length parameter  $r_0$ , which automatically regularizes the curve  $T_n$  in [Eq. \(9\)](#). For further comments on this approach see [Mergel et al. \(2019\)](#).

## 4 Examples of application

In the three following numerical examples we investigate the computational properties, robustness, and qualitative behavior of our two models. To demonstrate the generality of our method, we consider not only different dimensions (2D and 3D), but also different pairs of contact (rigid/deformable and deformable/deformable). A fourth, and more detailed, example follows in [Sect. 5](#), including a comparison with experiments and theoretical findings.

## 4.1 2D peeling of a thick strip from a rigid surface

We first consider a thick and beam-like strip, which is attached to a flat and rigid substrate as shown in Fig. 6. The lower surface of the strip is separated from the substrate by the equilibrium distance  $g_n = g_{eq}$  (see Fig. 2), so that the normal traction is initially zero. Peeling of the strip is initiated by moving the midpoint of its right boundary upwards.

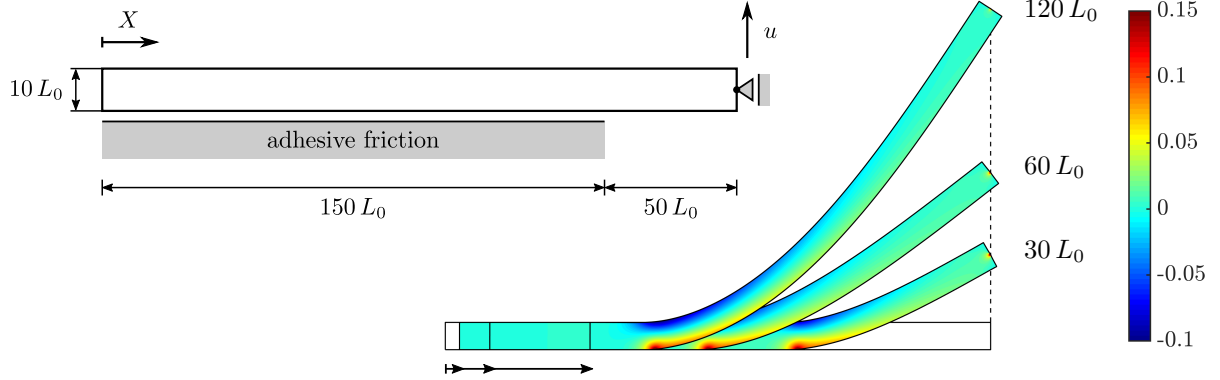


**Figure 6** 2D peeling of a strip: Problem setup (left) and peeling for model EA with  $s_{cut} = 1$  and  $\mu_{EA} = 0.01$  (right); the colors show  $\text{tr } \boldsymbol{\sigma} / E$ , where  $\boldsymbol{\sigma}$  is the Cauchy stress tensor.

Although this test case seems to be simple, it contains several computational challenges: First, for strong friction the strip partially remains sticking and stretches considerably before sliding. Second, the lower strip surface to the left of the peeling front remains close to its equilibrium position. This allows us to investigate the robustness of our friction models for this special case, in particular when the sliding threshold additionally contains a  $C^0$ -continuity at this position (Sect. 3.3).

In order to resolve the peeling zone and also to avoid shear locking due to bending (Wriggers, 2008), we discretize the bulk of the strip with  $320 \times 8$  quadratic finite elements. The contact surface is further enriched by quadratic NURBS shape functions (Corbett and Sauer, 2014). In this example, as well as in the following two subsections, we consider the Neo-Hooke material model stated in Bonet and Wood (1997). For the geometry, material, and contact parameters see Tab. 1. All results shown here are normalized by Young’s modulus  $E$ , an unspecified out-of-plane width  $W$ , and the unit length  $L_0$  (Fig. 6).

$E$	$\nu$	$A_H$	$r_0$	$L_0$
2 GPa	0.2	$10^{-19}$ J	0.4 nm	1 nm

**Table 1** 2D peeling of a strip: Model parameters.

### 4.1.1 Contact tractions

Fig. 6 illustrates the peeling of the strip for model EA and a small friction parameter. Fig. 7 shows the contact tractions for four configurations during the onset of peeling, once for model EA (with  $s_{cut} = 1$ , i.e.,  $g_{cut} = g_{max}$ ), and once for model DI (with  $g_{cut} = g_{max}$ ). As the comparison of Figs. 7(a) and 7(c) shows, the normal tractions are close to each other for both models in this specific setup. At the right boundary of the adhesive part, a sharp peeling front develops

(where  $T_n < 0$ ), and then propagates to the left during peeling. Next to this front, the contact traction is repulsive ( $T_n > 0$ ), caused by compression due to the bending stiffness of the strip. Together with the peeling front, Figs. 7(b) and 7(d) also show a sliding front propagating to the left. This front marks the transition between the strip surface remaining sticking and the strip surface already sliding. For model EA, the sliding traction distribution looks similar to the normal traction distribution (Figs. 7(a) and 7(b)). In contrast, the tangential traction during sliding is constant within the contact area for model DI (Fig. 7(d)). Since we here consider  $g_{\text{cut}} = g_{\text{max}}$  for both models, the sliding traction decreases to zero at  $|T_n| = T_{\text{max}}$ , implying sliding without friction beyond that point.

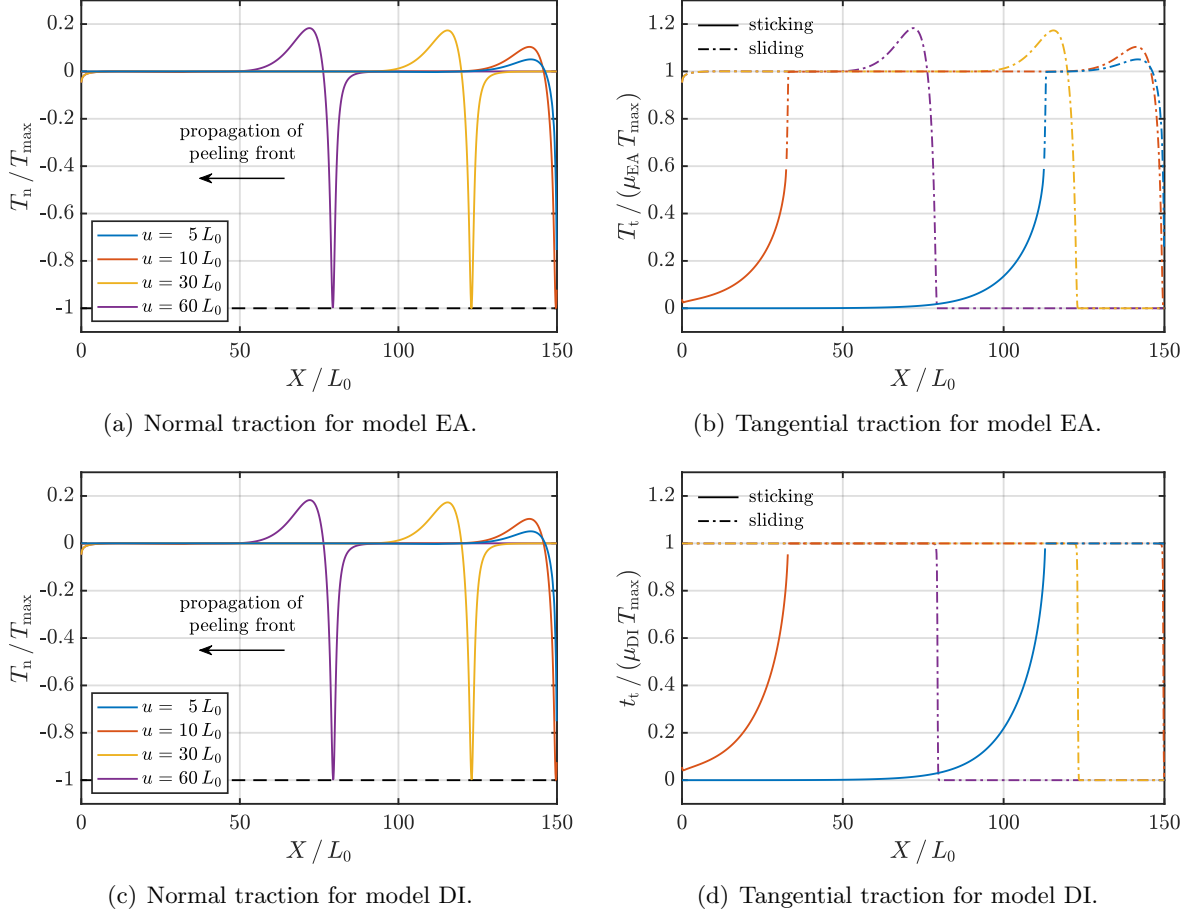


**Figure 7** 2D peeling of a strip: Traction at the contact area (in dependence of the horizontal position  $X$  normalized by  $L_0$ ) for models EA and DI with  $\mu_{\text{EA}} = \mu_{\text{DI}} = 0.01$  and  $g_{\text{cut}} = g_{\text{max}}$ ; the dash-dotted lines in Figs. (b) & (d) indicate sliding.

#### 4.1.2 Peeling forces

Let us first examine model EA (Sect. 2.3.3) in further detail. For this model the sliding traction distribution is proportional to the shifted normal traction. Figs. 8(a) and 8(b) show both the horizontal and vertical pull-off forces for two cutoff parameters,  $s_{\text{cut}} = 1$  and  $s_{\text{cut}} = 0.5$ , such that  $g_{\text{cut}} = g_{\text{max}}$  and  $g_{\text{cut}} = (g_{\text{eq}} + g_{\text{max}})/2$ . Note that the special case  $g_{\text{cut}} \rightarrow g_{\text{eq}}$  is discussed separately at the end of this example. With increasing friction parameter  $\mu_{\text{EA}}$ , large parts of the strip initially remain sticking to the substrate. The moment, at which full sliding is initiated,



appears as a kink in Figs. 8(a) and 8(b). As seen,  $\mu_{\text{EA}}$  seems to have a stronger influence than the cutoff distance  $g_{\text{cut}}$  (for  $g_{\text{cut}} > g_{\text{eq}}$ ).

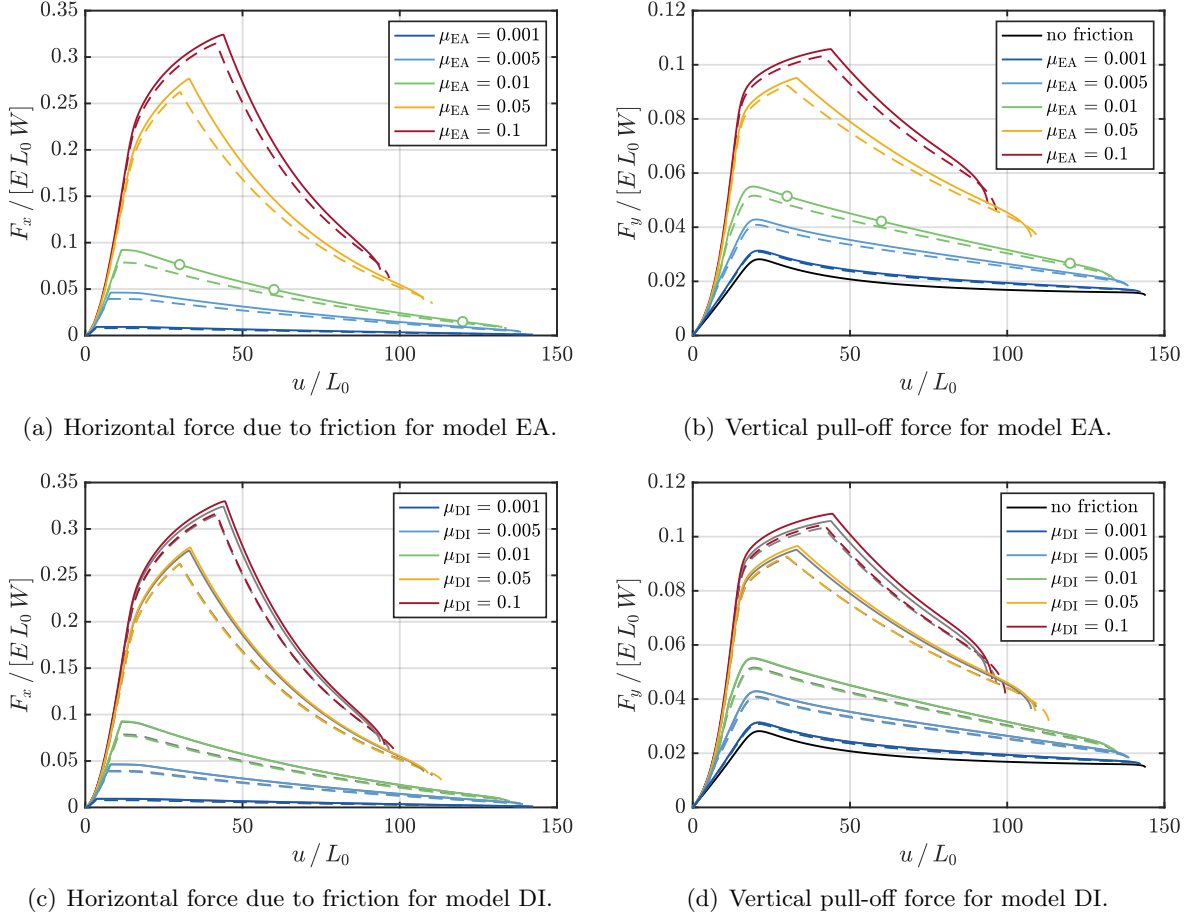


**Figure 8** 2D peeling of a strip: Forces in dependence of the vertical displacement for models EA and DI, both with  $g_{\text{cut}} = g_{\text{max}}$  (solid lines) and  $g_{\text{cut}} = (g_{\text{eq}} + g_{\text{max}})/2$  (dashed lines); the gray lines in Figs. (c) & (d) show the results of Figs. (a) & (b) for comparison; the circles mark the configurations plotted in Fig. 6.

We next examine model DI (Sect. 2.3.2) in further detail. In this model the sliding traction distribution is defined by the constant parameter  $\tau_{\text{DI}}$ . See also the definition  $\mu_{\text{DI}} = \tau_{\text{DI}} / T_{\text{max}}$  introduced in Sect. 2.3.2. For comparison we use the same cutoff distances as for model EA. Starting with  $g_{\text{cut}} = g_{\text{max}}$ , we observe in Figs. 8(c) and 8(d) that the results for models DI and EA match very well if  $\mu_{\text{DI}} = \mu_{\text{EA}}$ . The good agreement of the two models can be explained as follows: As can be seen in the contact tractions in Figs. 7(a) and 7(c), the attached part of the strip mainly remains at the equilibrium position,  $g_{\text{n}} = g_{\text{eq}}$ . At this distance, we obtain the following sliding thresholds when choosing  $g_{\text{cut}} = g_{\text{max}}$ :  $T_{\text{slide}}(g_{\text{eq}}) = \mu_{\text{EA}} T_{\text{max}}$  for model EA, and  $t_{\text{slide}}(g_{\text{eq}}) = \tau_{\text{DI}} = \mu_{\text{DI}} T_{\text{max}}$  for model DI. More generally, the two models show a similar behavior if (i) the surface stretches are small (such that  $J_{ck}, J_{cl} \approx 1$ , and thus  $\mathbf{t}_{t,k} \approx \mathbf{T}_{t,k}$ ), (ii) the contacting interfaces are mainly separated by the equilibrium distance  $g_{\text{eq}}$ , and (iii) if the model parameter are chosen as

$$g_{\text{eq}} < g_{\text{cut}} \leq g_{\text{max}}, \quad \mu_{\text{DI}} := \mu_{\text{EA}} \frac{|T_{\text{n}}(g_{\text{cut}})|}{T_{\text{max}}}. \quad (37)$$

This is demonstrated in Figs. 8(c) and 8(d) for  $g_{\text{cut}} = (g_{\text{eq}} + g_{\text{max}})/2$  and  $\mu_{\text{DI}}$  chosen according

to Eq. (37). In these figures, the maximum forces in the horizontal and vertical directions of the two models only differ by at most 1.96 % and 2.53 %, respectively. Note that models EA and DI will behave differently from each other if major parts of the contact area are in tension or compression, or if the surface stretch has a strong influence. This is discussed in the following examples. Further deviation may be caused by the regularization parameter  $k_{\text{DI}}$  of Eq. (14). For model DI the regularized traction law in Eq. (14) is  $C^1$ -continuous for arbitrary cutoff distances  $g_{\text{cut}}$ . In contrast, Eq. (16) for model EA has a kink at  $g_{\text{cut}}$  if  $g_{\text{cut}} \neq g_{\text{max}}$  (see e.g. Fig. 4(c)). Nevertheless, due to our active set and freezing strategy (Sect. 3.3), our algorithm works robustly for all cases investigated so far.

#### 4.1.3 Special case: Friction in compressed parts of the contact area

A special case is  $g_{\text{cut}} = g_{\text{eq}}$ , for which friction appears only in the compressed parts of the contact area. Model EA then resembles the classical Amontons-Coulomb law from Sect. 2.3.1 (see also the end of Sect. 2.3.3), while the unregularized form of model DI corresponds to the model by Deng et al. (2012). The normal gap that distinguishes between frictional and frictionless sliding now directly corresponds to the equilibrium distance  $g_{\text{eq}}$ . For low normal loads, this can lead to cycling and non-convergence (Sect. 3.3), as is discussed in the following.

	$s_{\text{cut}}$	$\mu_{\text{EA}} = 0.001$		$\mu_{\text{EA}} = 0.01$		$\mu_{\text{EA}} = 0.1$	
		$\Delta u$	$\Delta F_{\text{total}}$	$\Delta u$	$\Delta F_{\text{total}}$	$\Delta u$	$\Delta F_{\text{total}}$
$\varepsilon_t =  T'_n(g_{\text{eq}}) $	-0.01	4	0.05 %	4	0.55 %	4	6.92 %
	-0.001	4	0.01 %	4	0.07 %	4	0.91 %
	0	4	0.00 %	4	0.00 %	$< 1/32$	(cycling)
	0.001	$< 1/32$	(cycling)	$1/16$	0.38 %	1	5.19 %
	0.01	$1/16$	0.36 %	1	4.19 %	4	61.3 %
$\varepsilon_t =  T'_n(g_{\text{eq}}) /10$	-0.01	4	0.05 %	4	0.55 %	4	6.92 %
	-0.001	4	0.01 %	4	0.07 %	4	0.91 %
	0	4	0.00 %	4	0.00 %	$1/2$	0.00 %
	0.001	$1/16$	0.04 %	$1/8$	0.38 %	1	5.19 %
	0.01	$1/2$	0.36 %	1	4.19 %	4	61.3 %

**Table 2** 2D peeling of a strip: Largest possible numerical displacement increment  $\Delta u$  (in units of  $\Delta u_0 = 0.05 L_0$ ) for model EA to run stably with  $s_{\text{cut}} \approx 0$ , and two regularization parameters  $\varepsilon_t$ ;  $\Delta F_{\text{total}}$  denotes the relative difference of the maximum forces w.r.t.  $s_{\text{cut}} = 0$ ; the FE size is  $0.625 L_0 \times 1.25 L_0$ .

Tab. 2 shows the largest possible numerical displacement increment,  $\Delta u$ , that can be applied for this test case to run stably with model EA and cutoff parameters  $s_{\text{cut}}$  close to zero. For  $s_{\text{cut}} = 0$ ,  $\mu_{\text{EA}} = 0.1$ , and a regularization parameter of  $\varepsilon_t = |T'_n(g_{\text{eq}})|$  (the prime indicates the partial derivative w.r.t.  $g_n$ ), the friction algorithm runs into cycling even for a displacement step refined by factor 32. For small but positive cutoff parameters ( $s_{\text{cut}} = 0.001$  and  $s_{\text{cut}} = 0.01$ ), the friction algorithm is either still prone to cycling, or leads to a different behavior of the mechanical system, as becomes apparent in the relative difference  $\Delta F_{\text{total}}$  (w.r.t.  $s_{\text{cut}} = 0$ ). In contrast to this, small negative values like  $s_{\text{cut}} = -0.001$  yield both a robust algorithm and accurate results. As is also seen in Tab. 2, cycling can also be prevented by using a stronger regularization, i.e. a smaller value for  $\varepsilon_t$  in Eq. (28).<sup>5</sup> Note that both choices of  $\varepsilon_t$  used here

<sup>5</sup>In fact, we computed the reference forces in Tab. 2 for  $s_{\text{cut}} = 0$  with the reduced parameter  $\varepsilon_t = |T'_n(g_{\text{eq}})|/10$ .

lead to almost similar maximum forces. In any case, for both friction models the value of  $\varepsilon_t$  should be chosen in a reasonable manner compared to the considered friction parameter  $\mu_{\text{EA}}$  or  $\mu_{\text{DI}}$ , respectively (Mergel, 2017).

## 4.2 2D contact of two deformable cylinders

Next we study two deformable cylinders sliding along each other in 2D (Fig. 9(a)). Both cylinders have the same radius as well as the same material and contact properties (Tab. 3). For each cylinder we use approximately 1,500 elements and Hermite enrichment (Sauer, 2011) at the contact surfaces. As discussed in Sect. 2.2, the volume change at the surfaces is approximated by  $J_\ell \approx J_{c\ell}$  in Eq. (9). Since in this example (and for our choice of parameters)  $J_{c\ell}$  has only little influence (Mergel, 2017), we proceed with  $J_{c\ell} \approx 1$ .

$E$	$\nu$	$A_H$	$r_0$	$R$
1 GPa	0.3	$2.54 \cdot 10^{-20} \text{ J}$	0.4 nm	40 nm

**Table 3** 2D contact of two deformable cylinders: Model parameters.

Fig. 9(b) shows the two cylinders sliding across each other in the presence of frictionless adhesion. Here, the colors depict the absolute deviation of the first stress invariant,  $I_1 = \text{tr } \boldsymbol{\sigma}$ , from its average value (comparing all points in one body with their point-symmetric counterparts in the opposite body). Although the two-half-pass algorithm does not balance the contact tractions explicitly (Sauer and De Lorenzis, 2015), the stress fields of both bodies match to machine precision (see the scaling of the color bar). This agrees well with the results of Sauer and De Lorenzis (2015). As expected, we observe the same behavior in the test cases with friction, both for models DI and EA.

Figs. 9(c) and 9(d) show the deformation of the cylinders for models DI and EA using a large friction parameter. As these results demonstrate, the algorithm works robustly for both models (with ca. 4 to 9 Newton iterations in each load step) – even in the presence of a strong frictional resistance that results in large deformations. Fig. 10 shows the horizontal and vertical forces acting on the lower body for both models and different friction parameters. As seen, the friction forces for model DI are considerably smaller than for model EA. This is in particular due to the fact that in model DI the frictional forces depend on the normal forces implicitly, i.e., through an increasing contact area.

Note that in general, it depends on the specific application whether friction is more pressure- or adhesion-dominated; see e.g. the experimental results of Homola et al. (1990) for two mica cylinders sliding over each other. A detailed discussion of this topic can be found in Mergel et al. (2019).

## 4.3 3D peeling of a tape-like membrane

We now study 3D peeling of a soft and compliant tape (Fig. 11(a) and Tab. 4), which is modeled as a membrane (Sauer et al., 2014). Like other pure membrane models, this formulation only captures in-plane stresses, but does not account for any bending moments.

Initially, the entire lower surface of the tape is pre-stretched and attached to a rigid and motionless substrate. The pre-stretch of the tape is chosen as  $\lambda = 1.001$ . This is sufficient to avoid

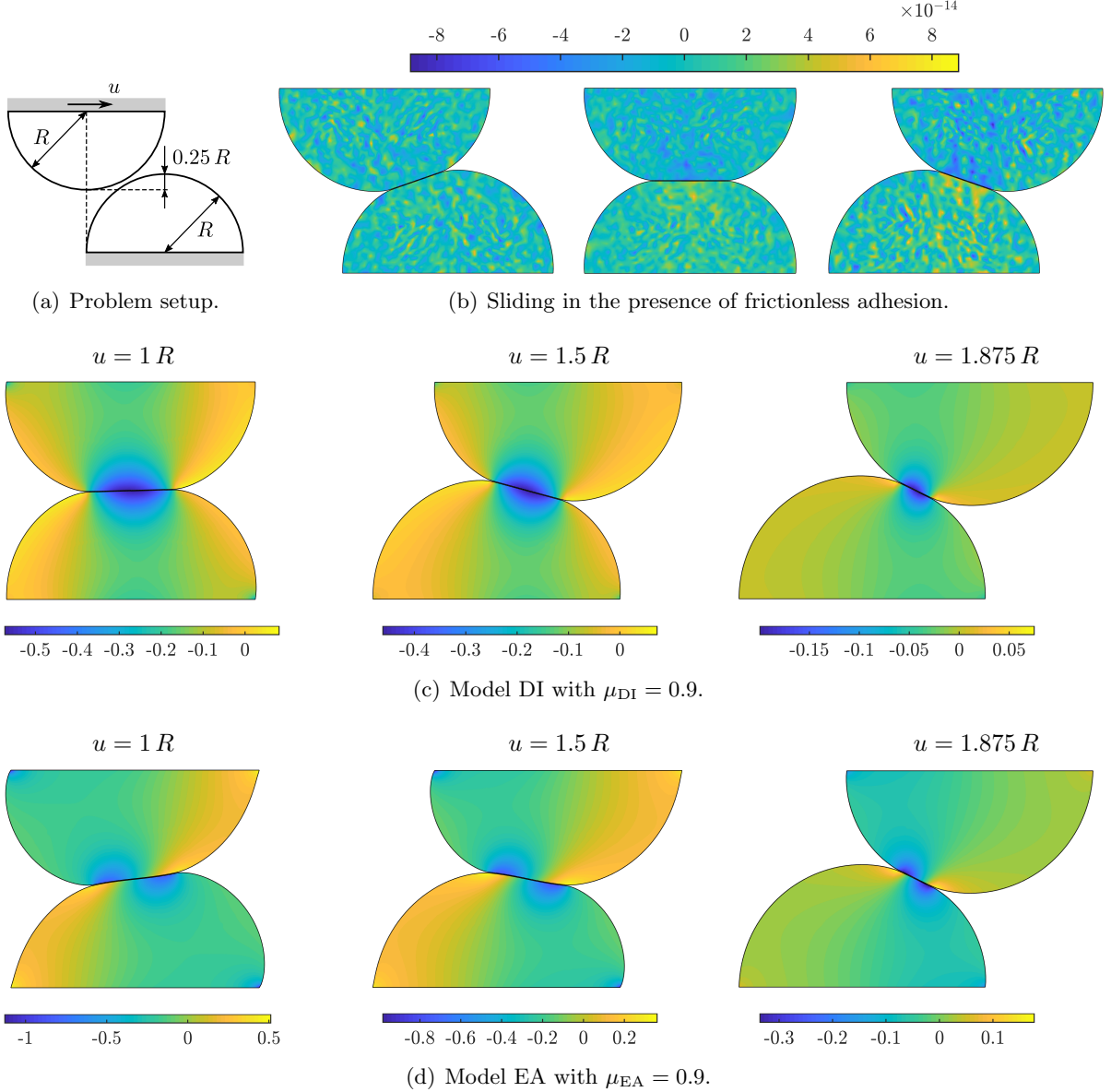


**Figure 9** 2D contact of two deformable cylinders: (a) Setup; (b) deformation during sliding for frictionless adhesion; the colors show the absolute deviation of  $\text{tr } \boldsymbol{\sigma} / E$  from its average value; (c) deformation during sliding for models DI and EA and  $g_{\text{cut}} = g_{\text{max}}$ ; the colors show  $\text{tr } \boldsymbol{\sigma} / E$ .

any local in-plane compression during peeling (which cannot be resisted by a pure membrane). The frictional sticking to the substrate prevents the tape from directly shrinking back to its un-stretched configuration. Afterwards, we start peeling off one side of the tape by prescribing a displacement along the angle  $\theta = 45^\circ$ . Note that this angle corresponds to the direction of motion, and not to the angle between the tape and the substrate at the peeling front.

Since (pure) membranes do not have any bending stiffness, the normal gap from Eq. (7) between the tape and the plane always satisfies  $g_n \geq g_{\text{eq}}$  during peeling. From Fig. 2 then follows that the normal contact traction is purely adhesive within the entire contact area. As a consequence, this particular setup cannot be investigated with friction models that yield a tangential resistance only under compression. Such models include both model EA with  $s_{\text{cut}} = 0$  (corresponding to the classical Amontons-Coulomb law for friction) and the model of Deng et al. (2012). Apart

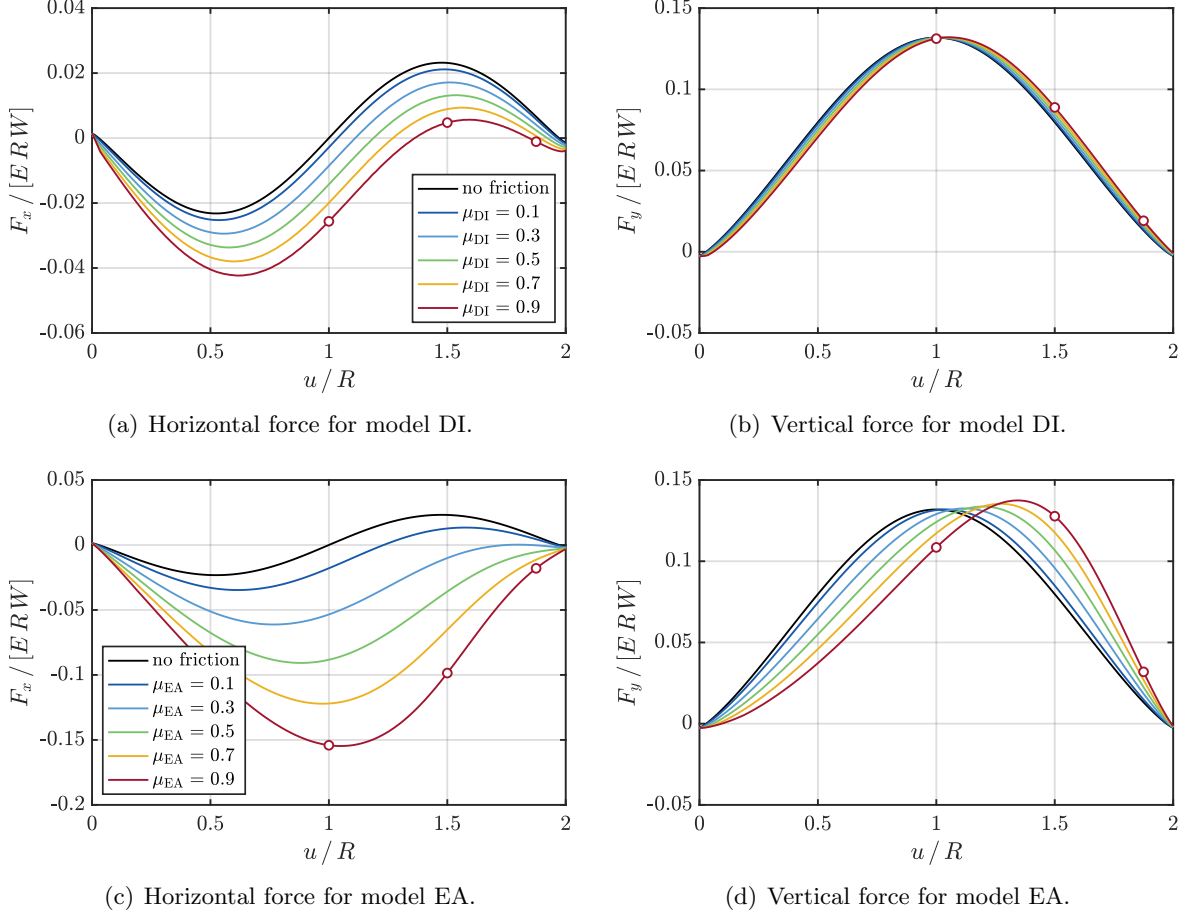


**Figure 10** 2D contact of two deformable cylinders: Forces acting on the lower body for models DI and EA, both with  $g_{\text{cut}} = g_{\text{max}}$ ; the dots mark the configurations shown in Fig. 9(c);  $W$  denotes the (unspecified) width or out-of-plane thickness of each cylinder.

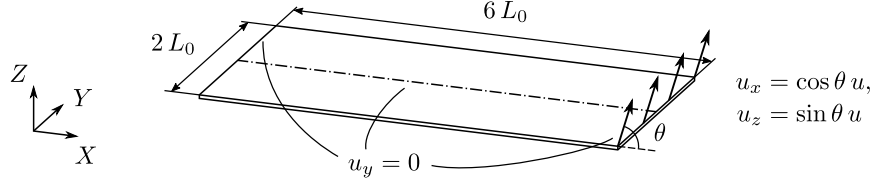
$E \cdot T$	$\nu$	$A_H$	$r_0$	$L_0$
0.02 N/m	0.3	$10^{-20}$ J	0.4 nm	1 nm

**Table 4** 3D peeling of a membrane: Model parameters.

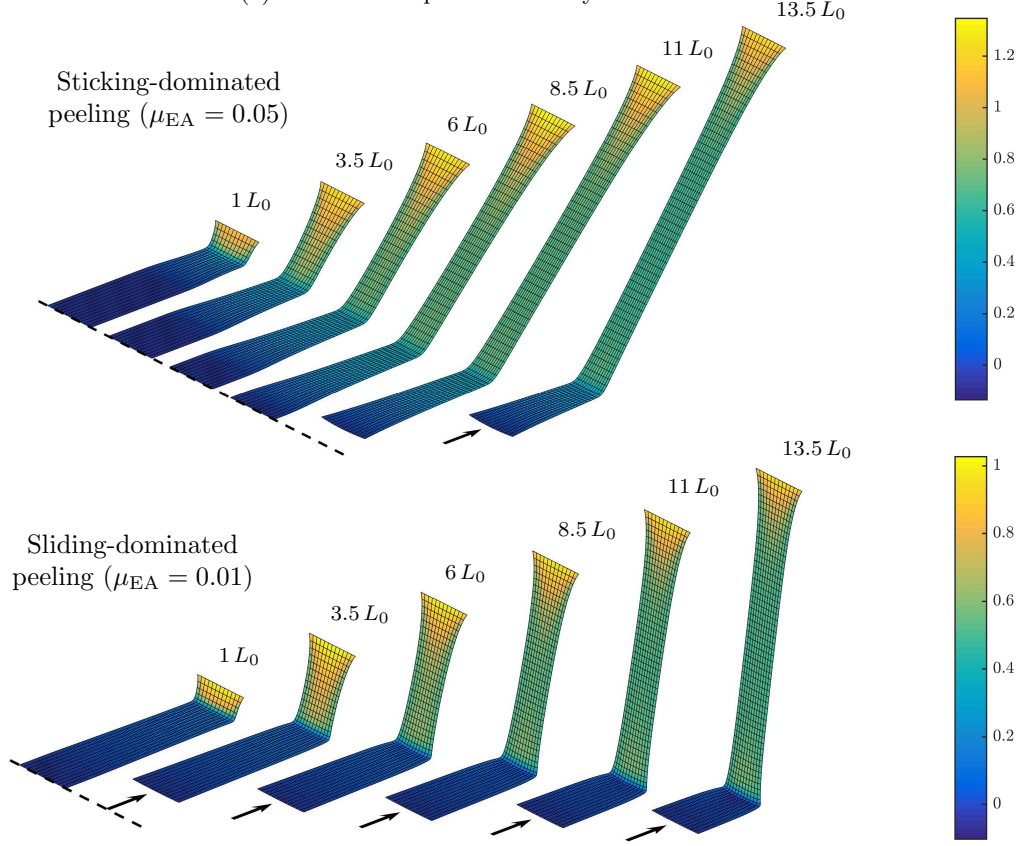
from that, even though it would be possible to model tangential sticking by means of a cohesive zone model, the membrane would slide without any frictional resistance after debonding.

The membrane is described by an incompressible Neo-Hooke material model (see Sauer et al. (2014)) with the parameters given in Tab. 4. This particular example is useful to demonstrate the computational behavior of our friction models and algorithms for extremely soft and compliant structures. To exploit the symmetry of the tape shown in Fig. 11(a), we discretize only one half of it by means of 540 quadratic NURBS elements (Sauer et al., 2014), and apply suitable boundary conditions along the center line.

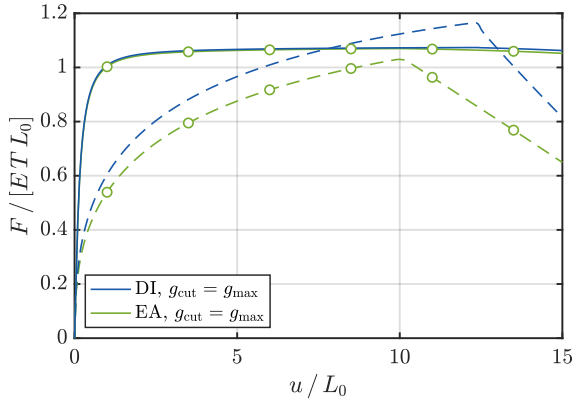
Fig. 11(b) shows the peeling process once for a large and once for a small friction parameter, leading either to strong sticking or immediate sliding. As can be seen in Figs. 11(c) and 11(d), in both cases the forces in the vertical direction are very close to each other for models EA and DI. The horizontal forces, however, are similar only for small friction. This is caused by the flexibility of the tape (see also Fig. 11(b) top), for which the surface stretch  $J_{ck}$  is not negligible



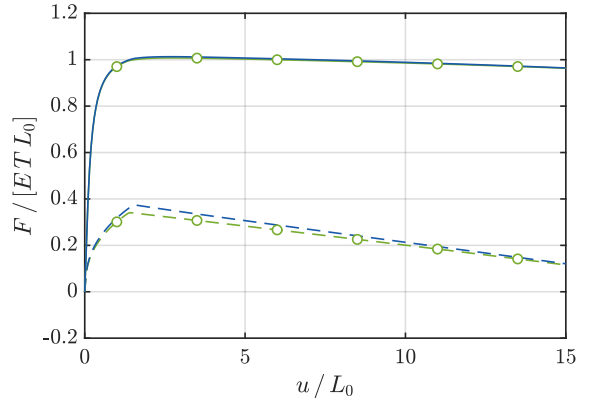
(a) Problem setup and boundary conditions.



(b) Detachment at  $\theta = 45^\circ$  dominated by either sticking (top) or sliding (bottom) for model EA and  $g_{\text{cut}} = g_{\text{max}}$ ; the colors show the logarithmic area stretch  $\ln J_c$ ; the figure shows both halves of the tape.



(c) Sticking-dominated peeling:  $\mu_{\text{EA}} = \mu_{\text{DI}} = 0.05$ .



(d) Sliding-dominated peeling:  $\mu_{\text{EA}} = \mu_{\text{DI}} = 0.01$ .

**Figure 11** 3D peeling of a membrane: (a) Setup; (b) detachment at  $\theta = 45^\circ$  for strong and weak friction; (c) & (d) forces in horizontal (dashed lines) and vertical (solid lines) directions for models EA and DI, the dots mark the configurations of Fig. (b).



anymore. It also explains the differences between the behavior observed here and the results from Sect. 4.1.2.

As this example demonstrates, we are able to model adhesive friction even for very soft structures exhibiting negligible bending stiffness. These include smooth adhesive pads of insects such as beetles. In particular, we are able to model frictional sliding during peeling of such structures, which would not be possible with conventional friction models or cohesive zone models.

## 5 Onset of frictional sliding for elastomer-like contact

Let us finally investigate adhesive friction between a smooth elastomer cap and a rigid substrate, as considered experimentally e.g. in [Sahli et al. \(2018\)](#) and [Mergel et al. \(2019\)](#), theoretically e.g. in [Papangelo and Ciavarella \(2019\)](#), and numerically considering linear elasticity ([Khajeh Salehani et al., 2019](#)). To this end, we bring a rigid plate into contact with a deformable, cylindrical cap by applying a constant normal force  $F_n$  (Fig. 12(a)). Due to adhesion between the cap and the plate, this force can be compressive, zero, or even slightly tensile. Keeping  $F_n$  constant, we then move the rigid plate horizontally, while keeping the lower boundary of the cap fixed.

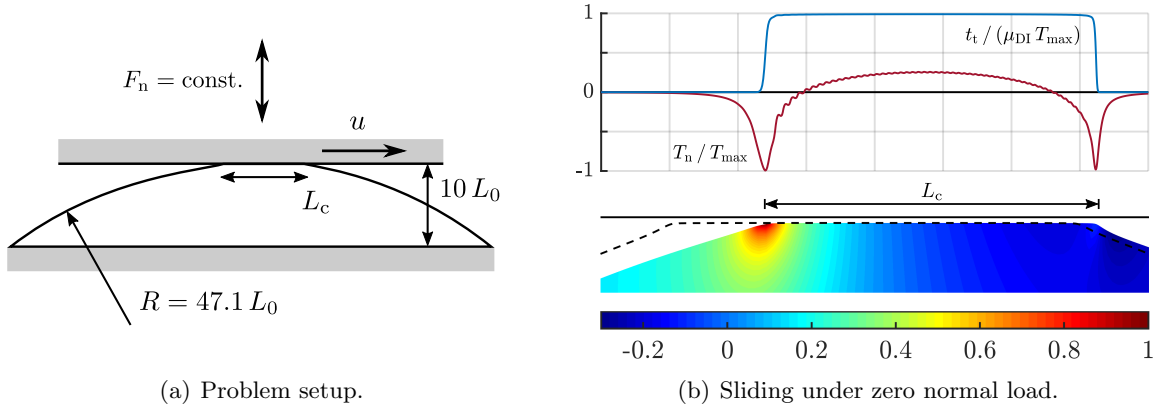


**Figure 12** Adhesive friction of a 2D cap: (a) Setup (the height of  $10 L_0$  refers to the undeformed cap before contact); (b) contact tractions (top panel) as well as deformation and stress distribution (bottom panel) at the interface during full sliding for  $F_n = 0$  according to model DI with  $g_{\text{cut}} = g_{\text{max}}$  and  $\mu_{\text{DI}} = 1$ ; the vertical axis of the deformation plot is stretched by factor 2; the colors show the first invariant of the Cauchy stress,  $\text{tr } \boldsymbol{\sigma} / E$ ; the dashed line indicates the contour of the cap before horizontal sliding ( $u = 0$ ).

Here, we use the same computational setup and parameters as in [Mergel et al. \(2019\)](#), which contains a short, preliminary study of the two models DI and EA. As demonstrated therein, model DI seems to be a promising candidate to investigate adhesive friction at smooth elastomer-glass interfaces. We further consider 2D plane-strain conditions, nonlinear Neo-Hookean material behavior ([Bonet and Wood, 1997](#)), and the model parameters from Tab. 5. The cap itself consists of 42,300 linear elements with quadratic NURBS enrichment on the contact surface ([Corbett and Sauer, 2014](#)). Our results are normalized by an out-of-plane unit width,  $W$ .



$E$	$\nu$	$T_{\max}$	$W_{\text{adh}}$	$L_0$
2 MPa	0.4	0.33 MPa	0.027 J/m <sup>2</sup>	1 $\mu\text{m}$

**Table 5** Adhesive friction of a 2D cap: Model parameters.

### 5.1 Adhesive friction between cap and substrate

Fig. 12(b) illustrates the contact interface deformation for sliding at  $F_n = 0$ , including the stress distribution in the bulk of the cap as well as the corresponding contact tractions. The negative peaks in the normal traction indicate adhesive stresses at the two contact edges. Fig. 13(a) shows the tangential force versus the prescribed displacement for different normal forces, while Fig. 13(b) depicts the corresponding contact length  $L_c$  (see Fig. 12(a)). The combination of both, i.e., the contact length in dependence of the tangential force, is shown in Fig. 13(c). Three of those curves (see the caption) were already shown in Mergel et al. (2019). We here confirm that for all investigated normal loads (compressive or tensile), the contact length is a decreasing function of the tangential force. By nature of model DI, this decrease stops when all points of the interface have reached the frictional shear strength  $\mu_{\text{DI}} T_{\max}$  (see the squares). This explains why all curves in Fig. 13(c) end at the dotted line.

For the two lowest initial contact lengths (black solid lines in Figs. 13(a) to 13(c)), the computations terminate even for small displacement increments. The most likely explanation is that for these cases, the tensile normal force is sufficiently large so that the cap snaps from the substrate before full tangential sliding. This behavior can also be observed in experiments (Waters and Guduru, 2010; Mergel et al., 2019). In order to confirm our hypothesis, we consider the generalized plane strain JKR model by Chen et al. (2008), and compute the critical length  $L_{\text{detach}}$  for which the cap detaches from the substrate. Inserting the parameters from Tab. 5, we obtain  $L_{\text{detach}} = 4.53 L_0$ , which is very close to the detachment lengths observed in our simulations (see the dashed black lines and the black crosses in Figs. 13(b) and 13(c)).

Let us now compare our results with experiments on shearing of smooth elastomer spheres on glass plates. As explained in detail in Mergel et al. (2019), these comparisons are only qualitative for now due to length scale differences between experiments (mm range) and computations ( $\mu\text{m}$  range) related to the adhesion model by Sauer and Wriggers (2009). In such experiments, the initially circular contact area shrinks to an ellipse during the onset of sliding (Mergel et al., 2019; Sahli et al., 2018, 2019). Sahli et al. (2019) demonstrated experimentally that

- 1) the width of the contact area *perpendicular* to the direction of sliding nearly remains constant; and
- 2) the length  $L_c$  *parallel* to the direction of sliding is well-captured by the quadratic fit

$$L_c(F_t) = L_{c,0} - \xi F_t^2. \quad (38)$$

In Eq. (38),  $L_{c,0}$  is the initial contact length (at  $F_t = 0$ ), and  $\xi$  is a parameter that is independent from  $F_t$ , but depends on the applied normal load, or equivalently the initial contact area.

As the dash-dotted lines in Fig. 13(c) indicate, Eq. (38) is also well-suited to fit the curves from our numerical results, using the least-squares method. Although the caps in the experiments by Sahli et al. (2019) and those in our simulations have different dimensions (spherical in the experiments vs. cylindrical in the simulations), we observe consistent behavior. This motivates us investigating whether the dependence of the parameter  $\xi$  on the initial contact length/area

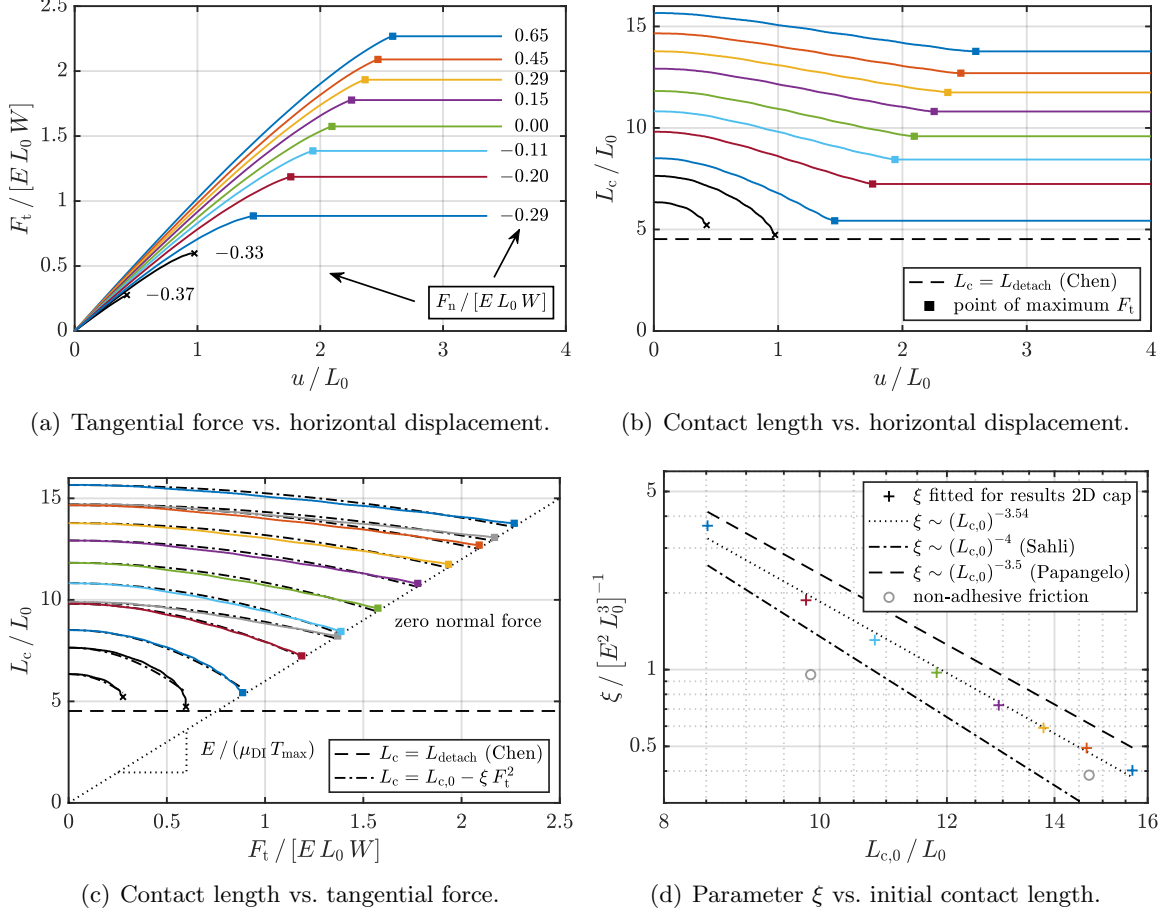


**Figure 13** Adhesive friction of a 2D cap: (a) & (b) Tangential force and contact length, respectively, obtained for model DI ( $g_{\text{cut}} = g_{\text{max}}$ ,  $\mu_{\text{DI}} = 1$ ) and different normal forces; the orange, green and lower dark blue lines correspond to the cases shown in Mergel et al. (2019); the two solid black lines indicate unstable (vanishing) contact; (c) contact length in dependence of the tangential force; the two grey lines correspond to non-adhesive friction (Sect. 5.2); (d) parameter  $\xi$  from Eq. (38) fitted for the cases from Fig. (c) with stable contact.

is similar, too. Sahli et al. (2019) observe for their experiments  $\xi(A_{c,0}) \sim A_{c,0}^{-2}$ , with  $A_{c,0}$  being the (circular) initial contact area. Regarding the initial contact length  $L_{c,0}$ , this translates with  $A_{c,0} \sim L_{c,0}^2$  into  $\xi(L_{c,0}) \sim L_{c,0}^{-4}$ . For comparison, Fig. 13(d) shows the parameter  $\xi$  fitted for our numerical results in dependence of  $L_{c,0}$ . As can be seen, these data are also linear with logarithmic scales. Our simulations yield  $\xi(L_{c,0}) \sim L_{c,0}^\beta$  with  $\beta = -3.54$ , which is in good agreement with the  $-4$  inferred from Sahli et al. (2019).

Note that the experimental results by Sahli et al. (2018, 2019) also match well with the fracture-mechanics models by Papangelo and Ciavarella (2019) and Papangelo et al. (2019). Those models describe the evolution of the contact area of adhesive sphere-plane contact under shear, assuming either a circular or an elliptic contact area, respectively. For an initially circular area and for small  $F_t$ , Papangelo and Ciavarella (2019) predict the relation  $A_c(F_t) = A_{c,0} - \alpha F_t^2$  with  $\alpha(A_{c,0}) \sim A_{c,0}^{-5/4}$ . This equation can be related to the parameter  $\xi$  from Eq. (38) as follows: Motivated by their experiments, Sahli et al. (2019) assume that the contact area shrinks only along the shear direction and has an elliptic shape afterwards. With these two assumptions, the authors show that the exponents of  $\alpha$  and  $\xi$  differ by the value  $-1/2$ , so that one expects

$\xi(A_{c,0}) \sim A_{c,0}^{-7/4}$ . This, in turn, translates into  $\xi(L_{c,0}) \sim L_{c,0}^{-7/2}$ , which is remarkably close to the  $-3.54$  fitted for our numerical results (Fig. 13(d)). In summary, our exponent  $\beta$  lies in between the two values observed experimentally and determined theoretically.

Motivated by this good agreement, we investigate another finding by Papangelo et al. (2019). The authors conclude that the contact area does not always decrease as  $F_t^2$ , but rather as  $F_t^\eta$ , where  $\eta$  is an exponent depending also on the normal load.  $\eta$  is found to be close to 2 only for sufficiently large normal loads (such as those applied in Sahli et al. (2018, 2019)), while increasing with smaller loads. To test whether our simulations produce a similar behavior, in Fig. 14(a) we plot the evolution of  $(1 - L_c / L_{c,0})$  as a function of  $F_t$ . We here consider all normal forces used in Fig. 13 (except those for which the contact area vanishes before full sliding). For each normal force, the curves are linear in logarithmic scales, indicating that indeed  $(1 - L_c / L_{c,0}) \sim F_t^\eta$ . The least-square fitting of  $\eta$  to the numerical results is shown as dashed lines in Fig. 14(a).

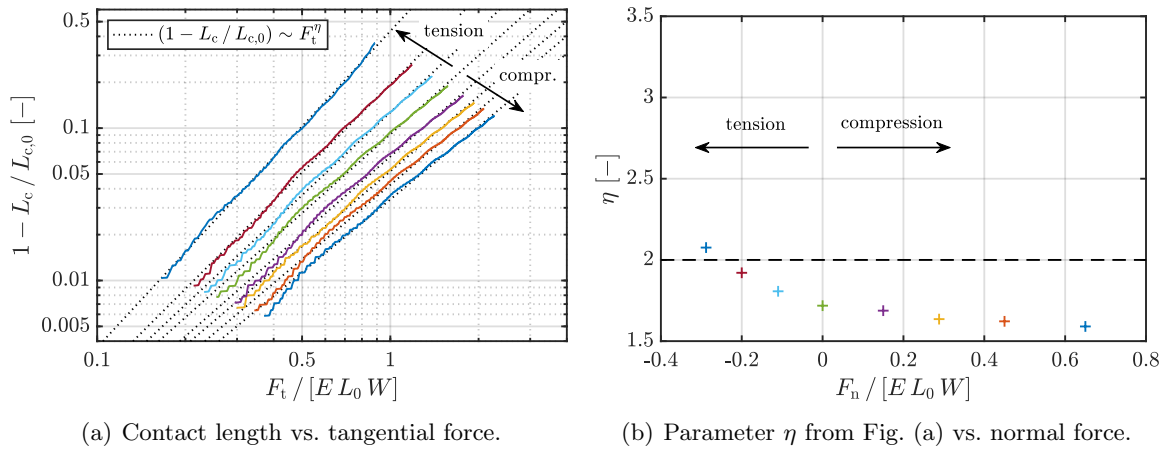


**Figure 14** Adhesive friction of a 2D cap: (a) Logarithmic representation of the contact length in dependence of the tangential force as considered in Papangelo et al. (2019); the figure shows only those cases from Fig. 13(d) with stable (non-vanishing) contact; (b) fitting of the parameter  $\eta$  to the relation  $(1 - L_c / L_{c,0}) \sim F_t^\eta$  (indicated in (a) as dotted lines).

Fig. 14(b) shows the evolution of the fitted exponent  $\eta$  as a function of the normal force  $F_n$ . In our simulations,  $\eta$  is close to 2 for the smallest normal loads, explaining why the quadratic fit in Fig. 13(c) is rather good for these cases. For increasing  $F_n$ , the exponent monotonously decreases and then approaches 1.5. This also explains the larger differences in the quadratic fits for those loads (Fig. 13(c)). Overall, both plots in Fig. 14 are in good qualitative agreement with those of Fig. 10 in Papangelo et al. (2019). To conclude, even though we have different contact dimensions here, our 2D simulations agree very well with both experiments (Sahli et al., 2018, 2019) and theoretical models (Papangelo and Ciavarella, 2019; Papangelo et al., 2019) for adhesive friction of smooth elastomer spheres and glass plates.

## 5.2 Investigation of non-adhesive friction

The two above-mentioned theoretical models suggest that in the absence of adhesion, the contact area would not decrease under shear. With our numerical model, we are able to test this hypothesis under more realistic assumptions, such as large deformations or adhesion and friction described explicitly rather than being lumped in a phenomenological mode-mixity parameter.

We thus consider two additional test cases (with two different initial contact lengths) without adhesion, simply setting the normal traction  $T_n$  in Eq. (9) and Fig. 3(a) to zero for  $g_n > g_{\text{cut}}$ . The corresponding results are shown as grey lines and circles in Figs. 13(c) and 13(d), respectively. We here consider initial contact lengths close to two of those obtained with adhesion (orange and dark red curves). Note that the normal force required to obtain the same contact length is considerably larger for the non-adhesive than for the adhesive case.

As Fig. 13(c) shows, the contact length decreases under tangential shear even in the absence of adhesion. In addition, the curves still seem to be well-fitted by the quadratic decay (38). Compared to the adhesive case, the decrease in  $L_c$  is lower, resulting in smaller values for the parameter  $\xi$  (Fig. 13(d)). If we assumed that  $\xi$  would also follow a power law of the form  $\xi(L_{c,0}) \sim L_{c,0}^\beta$ , its exponent would correspond to  $\beta = -2.28$  (instead of  $-3.54$  with adhesion). In contrast to the prevailing view in the literature, our results indicate that the shear-induced decrease of the contact length does not result from adhesion only. Although adhesion may enhance the magnitude of this effect, the observed decrease is expected to mainly result from the nonlinear deformation of the cap. Testing the validity of such a conclusion for 3D sphere-plane contact would be a promising topic for future work, but is beyond the scope of this paper.

## 6 Conclusion

This work provides a computational framework for two theoretical continuum models recently proposed for dry adhesion and friction (Mergel et al., 2019). These models are applicable to natural and technical systems, in which friction is either considerably influenced or purely dominated by adhesive effects. Up to a certain distance of the adhering surfaces, both models capture friction even for zero or tensile contact tractions. This distinguishes our models from existing approaches. It is motivated by soft bio-adhesive pads that are able to generate friction even under tensile normal loads.

While Mergel et al. (2019) contains the theory behind the two models DI and EA as well as new experimental results, in this paper we derive the corresponding model equations in terms of a 3D finite element (FE) formulation based on large-deformation continuum mechanics. We then describe the algorithmic treatment of sticking and sliding friction, using the unbiased friction algorithm by Sauer and De Lorenzis (2015). Afterwards, we state the resulting contact FE forces as well as their tangent matrices for two deformable solids in 3D. Note that there also exists an adaptation of models DI and EA to a geometrically exact beam formulation (Sauer and Mergel, 2014); see Mergel (2017).

In various numerical examples, we here investigate the properties of our friction models, focusing on numerical aspects first. The considered systems range from structures with high stiffness to soft and flexible tapes. Note that if the bending stiffness of such tapes is negligible, sliding friction cannot be modeled with existing approaches like cohesive zone or other friction models. We finally study an example that is inspired by the onset of sliding of Hertz-like elastomer-glass contact. To this end, we investigate friction of a soft cap and a rigid plate to compare our results both with experimental findings (Sahli et al., 2018, 2019) and theoretical investigations (Chen et al., 2008; Papangelo and Ciavarella, 2019; Papangelo et al., 2019). As these results demonstrate, our model is able to capture remarkably well the qualitative behavior of smooth elastomer-glass interfaces. Our results also suggest that adhesion is not the only mechanism responsible for shear-induced area reduction of such interfaces. Instead, this is rather an effect of the nonlinear material behavior. These results contribute to the current debate on the shear-induced area-reduction in elastomer contact (tribonet.org, 2019).

Motivated by our results, it would be promising to compare our models also with experimental results for horizontal tape peeling of elastomer strips from glass (Ponce et al., 2015). As demonstrated in the following references, our friction models are also suitable to investigate peeling of gecko spatulae (Mergel, 2017; Gouravaraju et al., 2019) or “friction hairs” at the feet of insects (Mergel, 2017). An initial investigation of such hairs confirms the assumption of Labonte et al. (2014) that their conical shape tends to facilitate a fast and controllable detachment.

## A Tangent matrices for adhesive and frictional contact

This section summarizes the tangent matrices that are required for the linearization of the contact terms in the governing equations (Sect. 3). For details on the derivation of these matrices we refer to Sauer and De Lorenzis (2013, 2015) and Mergel (2017).

As becomes apparent in Fig. 1, the normal gap  $g_n$ , and hence also the elemental contact force  $\mathbf{f}_{c,k}^e = \mathbf{f}_{n,k}^e - \mathbf{f}_{t,k}^e$ , depend on the surfaces of both interacting bodies,  $k, \ell = 1, 2, k \neq \ell$ . For linearization we thus need the following two tangent matrices

$$\mathbf{k}_{c,kk}^e = \frac{\partial \mathbf{f}_{c,k}^e}{\partial \mathbf{u}_k^e}, \quad \mathbf{k}_{c,k\ell}^e = \frac{\partial \mathbf{f}_{c,k}^e}{\partial \mathbf{u}_\ell^e}, \quad (39)$$

where the vector  $\mathbf{u}_k^e$  contains the nodal displacements for element  $\Gamma_{ck}^e$ , and  $\mathbf{u}_\ell^e$  is the displacement vector of all elements  $\Gamma_{c\ell}^e$  that are affected by  $\Gamma_{ck}^e$ . In analogy to Eq. (34), the tangent matrices in Eq. (39) can be decomposed into the contributions  $\mathbf{k}_{c,kk}^e = \mathbf{k}_{n,kk}^e - \mathbf{k}_{t,kk}^e$  and  $\mathbf{k}_{c,k\ell}^e = \mathbf{k}_{n,k\ell}^e - \mathbf{k}_{t,k\ell}^e$ .

### A.1 Tangent matrices for normal (adhesive and repulsive) contact

For normal contact (Sect. 2.2) with  $\theta_k \equiv 1$  and  $J_\ell \approx J_{c\ell}$ , the first matrix is given by

$$\mathbf{k}_{n,kk}^e = - \int_{\Gamma_{c0k}^e} \mathbf{N}_k^T \frac{\partial T_{n,k}}{\partial \mathbf{x}_k} \mathbf{N}_k \, dA_k, \quad (40)$$

where

$$\frac{\partial T_{n,k}}{\partial \mathbf{x}_k} = \frac{T'_n}{J_{c\ell}^e} \mathbf{n}_p \otimes \mathbf{n}_p + \frac{T_n}{J_{c\ell}^e} \frac{\partial \mathbf{n}_p}{\partial \mathbf{x}_k} - \frac{T_n}{(J_{c\ell}^e)^2} \mathbf{n}_p \otimes \frac{\partial J_{c\ell}^e}{\partial \mathbf{x}_k}, \quad (41)$$

and

$$T'_n = \frac{\partial T_n}{\partial g_n} = -\frac{A_H}{2\pi r_0^4} \left[ \frac{1}{5} \left( \frac{r_0}{g_n} \right)^{10} - \left( \frac{r_0}{g_n} \right)^4 \right], \quad (42)$$

$$\frac{\partial \mathbf{n}_p}{\partial \mathbf{x}_k} = \frac{1}{g_n} \left[ \mathbf{1} - \mathbf{n}_p \otimes \mathbf{n}_p - c_p^{\alpha\beta} \mathbf{a}_\alpha^p \otimes \mathbf{a}_\beta^p \right]. \quad (43)$$

The scalar  $J_{c\ell}^e$  is the surface stretch at projection point  $\mathbf{x}_p$ :  $J_{c\ell}^e = \|\mathbf{a}_1^p \times \mathbf{a}_2^p\| / \|\mathbf{A}_1^p \times \mathbf{A}_2^p\|$  (see also Eq. (10)). The derivative of  $J_{c\ell}^e$  with respect to  $\mathbf{x}_k$  can be computed from

$$\frac{\partial J_{c\ell}^e}{\partial \mathbf{x}_k} = J_{c\ell,\alpha}^e c_p^{\alpha\beta} \mathbf{a}_\beta^p, \quad J_{c\ell,\alpha}^e := \frac{\partial J_{c\ell}^e}{\partial \xi_\alpha^p} = J_{c\ell}^e \left[ \mathbf{a}_p^\beta \cdot \frac{\partial \mathbf{a}_\beta^p}{\partial \xi_\alpha^p} - \mathbf{A}_p^\beta \cdot \frac{\partial \mathbf{A}_\beta^p}{\partial \xi_\alpha^p} \right]. \quad (44)$$

In Eq. (43),  $\mathbf{1}$  denotes the identity tensor,  $\mathbf{a}_\alpha^p$  and  $\mathbf{n}_p$  are given by Eqs. (3) and (5), and  $c_p^{\alpha\beta}$  are the components of the matrix

$$[c_p^{\alpha\beta}] = \left[ a_{\alpha\beta}^p - g_n (\mathbf{n}_p \cdot \mathbf{a}_{\alpha,\beta}^p) \right]^{-1}, \quad \mathbf{a}_{\alpha,\beta}^p = \frac{\partial \mathbf{a}_\alpha(\boldsymbol{\xi})}{\partial \xi_\beta^p} \bigg|_{\boldsymbol{\xi}=\boldsymbol{\xi}_p}; \quad (45)$$

see Eq. (4). The second tangent matrix, containing the derivatives with respect to the neighboring nodes  $\mathbf{u}_\ell^e$ , is determined from

$$\mathbf{k}_{n,k\ell}^e = - \int_{\Gamma_{c0k}^e} \mathbf{N}_k^T \frac{\partial \mathbf{T}_{n,k}}{\partial \mathbf{u}_\ell^e} dA_k \quad (46)$$

and

$$\frac{\partial \mathbf{T}_{n,k}}{\partial \mathbf{u}_\ell^e} = - \frac{\partial \mathbf{T}_{n,k}}{\partial \mathbf{x}_k} \mathbf{N}_\ell - \frac{T_n}{J_{cl}^e} \left[ c_p^{\alpha\beta} \mathbf{a}_\alpha^p \otimes \mathbf{n}_p + \mathbf{n}_p \otimes \mathbf{a}_p^\beta + g_n \frac{J_{cl,\alpha}^e}{J_{cl}^e} c_p^{\alpha\beta} \mathbf{n}_p \otimes \mathbf{n}_p \right] \mathbf{N}_{\ell,\beta}. \quad (47)$$

In Eq. (47),  $\mathbf{N}_{\ell,\beta}$  contains the partial derivatives of the nodal shape functions  $\mathbf{N}_\ell$  with respect to coordinate  $\xi^\beta$ .

## A.2 Tangent matrices for tangential (sticking and sliding) contact

For a friction model stated in the *reference* configuration (like model EA), the associated tangent matrices have a form that is very similar to Eqs. (40) and (46):

$$\mathbf{k}_{t,kk}^e = - \int_{\Gamma_{c0k}^e} \mathbf{N}_k^T \frac{\partial \mathbf{T}_{t,k}}{\partial \mathbf{x}_k} \mathbf{N}_k dA_k, \quad \mathbf{k}_{t,k\ell}^e = - \int_{\Gamma_{c0k}^e} \mathbf{N}_k^T \frac{\partial \mathbf{T}_{t,k}}{\partial \mathbf{u}_\ell^e} dA_k. \quad (48)$$

In contrast, for a model in the *current* configuration (like model DI), we must additionally linearize the surface stretch appearing in  $da_k = J_{ck}^e dA_k$ ; this leads to a second term in  $\mathbf{k}_{t,kk}^e$ ,

$$\mathbf{k}_{t,kk}^e = - \int_{\Gamma_{ck}^e} \mathbf{N}_k^T \frac{\partial \mathbf{t}_{t,k}}{\partial \mathbf{x}_k} \mathbf{N}_k da_k - \int_{\Gamma_{ck}^e} \mathbf{N}_k^T \mathbf{t}_{t,k} \otimes \mathbf{a}_k^\alpha \mathbf{N}_{k,\alpha} da_k, \quad (49)$$

$$\mathbf{k}_{t,k\ell}^e = - \int_{\Gamma_{ck}^e} \mathbf{N}_k^T \frac{\partial \mathbf{t}_{t,k}}{\partial \mathbf{u}_\ell^e} da_k, \quad (50)$$

see e.g. Sauer and De Lorenzis (2015). The partial derivatives appearing in Eqs. (48) to (50) are specified in the following for both sticking and sliding friction. Unless stated otherwise, all quantities are evaluated at the current pseudo-time step,  $t_{n+1}$ ; see Sect. 3.1. Like in that section, we first discuss the case for which the traction is defined in the current configuration.

### A.2.1 Sticking friction

During sticking, the tangential traction corresponds to the elastic trial value  $\mathbf{t}_{\text{trial}}$ ; see Eqs. (28) and (30). The derivatives of this trial value with respect to both  $\mathbf{u}_k^e$  and  $\mathbf{u}_\ell^e$  are given by

$$\frac{\partial \mathbf{t}_{\text{trial}}}{\partial \mathbf{x}_k} = \varepsilon_t c_p^{\alpha\beta} \mathbf{a}_\alpha^p \otimes \mathbf{a}_\beta^p, \quad (51)$$

$$\frac{\partial \mathbf{t}_{\text{trial}}}{\partial \mathbf{u}_\ell^e} = - \frac{\partial \mathbf{t}_{\text{trial}}}{\partial \mathbf{x}_k} \mathbf{N}_\ell(\boldsymbol{\xi}_p) + \varepsilon_t [\mathbf{N}_\ell(\boldsymbol{\xi}_p) - \mathbf{N}_\ell(\boldsymbol{\xi}_s^n)] + \varepsilon_t g_n c_p^{\alpha\beta} \mathbf{a}_\alpha^p \otimes \mathbf{n}_p \mathbf{N}_{\ell,\beta}(\boldsymbol{\xi}_p). \quad (52)$$

Regarding a model in the reference configuration, one obtains the same two expressions for  $\partial \mathbf{T}_{\text{trial}} / \partial \mathbf{u}_k^e$  and  $\partial \mathbf{T}_{\text{trial}} / \partial \mathbf{u}_\ell^e$ , but with a penalty parameter that refers to the *reference* area,  $dA_k$ .

### A.2.2 Sliding friction

During sliding, the contact traction satisfies Eq. (26). After introducing

$$\mathbf{p}_t = \frac{t_{\text{slide}}}{\|\mathbf{t}_{\text{trial}}\|} [\mathbf{1} - \mathbf{n}_t \otimes \mathbf{n}_t], \quad \mathbf{n}_t = \frac{\mathbf{t}_{\text{trial}}}{\|\mathbf{t}_{\text{trial}}\|}, \quad (53)$$

and using Eqs. (51) and (52), we obtain

$$\frac{\partial \mathbf{t}_{t,k}}{\partial \mathbf{x}_k} = \mathbf{p}_t \frac{\partial \mathbf{t}_{\text{trial}}}{\partial \mathbf{x}_k} + \mathbf{n}_t \otimes \frac{\partial t_{\text{slide}}}{\partial \mathbf{x}_k}, \quad (54)$$

$$\frac{\partial \mathbf{t}_{t,k}}{\partial \mathbf{u}_\ell^e} = \mathbf{p}_t \frac{\partial \mathbf{t}_{\text{trial}}}{\partial \mathbf{u}_\ell^e} + \mathbf{n}_t \otimes \frac{\partial t_{\text{slide}}}{\partial \mathbf{u}_\ell^e}. \quad (55)$$

In analogy, we obtain for the reference configuration

$$\frac{\partial \mathbf{T}_{t,k}}{\partial \mathbf{x}_k} = \mathbf{P}_t \frac{\partial \mathbf{T}_{\text{trial}}}{\partial \mathbf{x}_k} + \mathbf{N}_t \otimes \frac{\partial T_{\text{slide}}}{\partial \mathbf{x}_k}, \quad (56)$$

$$\frac{\partial \mathbf{T}_{t,k}}{\partial \mathbf{u}_\ell^e} = \mathbf{P}_t \frac{\partial \mathbf{T}_{\text{trial}}}{\partial \mathbf{u}_\ell^e} + \mathbf{N}_t \otimes \frac{\partial T_{\text{slide}}}{\partial \mathbf{u}_\ell^e}, \quad (57)$$

where

$$\mathbf{P}_t = \frac{T_{\text{slide}}}{\|\mathbf{T}_{\text{trial}}\|} [\mathbf{1} - \mathbf{N}_t \otimes \mathbf{N}_t], \quad \mathbf{N}_t = \frac{\mathbf{T}_{\text{trial}}}{\|\mathbf{T}_{\text{trial}}\|}. \quad (58)$$

The derivatives in Eqs. (54) to (57) are either stated in App. A.2.1, or they are specified next.

### A.2.3 Partial derivatives of the sliding threshold

- 1) Model DI (Sect. 2.3.2): The partial derivatives of  $t_{\text{slide}}$  from Eq. (14) are given by

$$\frac{\partial t_{\text{slide}}}{\partial \mathbf{x}_k} = t'_{\text{slide}}(g_n) \mathbf{n}_p, \quad \frac{\partial t_{\text{slide}}}{\partial \mathbf{u}_\ell^e} = -t'_{\text{slide}}(g_n) \mathbf{N}_\ell^T \mathbf{n}_p, \quad (59)$$

where

$$t'_{\text{slide}}(g_n) = \frac{\partial t_{\text{slide}}}{\partial g_n} = \frac{\tau_{\text{DI}} k_{\text{DI}}}{1 + e^{k_{\text{DI}}(g_n - g_{\text{cut}})}} \left[ \frac{1}{1 + e^{k_{\text{DI}}(g_n - g_{\text{cut}})}} - 1 \right]. \quad (60)$$

- 2) Model EA (Sect. 2.3.3): From Eq. (16) follows that

$$\frac{\partial T_{\text{slide}}}{\partial \mathbf{x}_k} = \frac{\mu_{\text{EA}}}{J_{\text{cl}}^e} T'_n(g_n) \mathbf{n}_p - \frac{T_{\text{slide}}}{J_{\text{cl}}^e} \frac{\partial J_{\text{cl}}^e}{\partial \mathbf{x}_k}, \quad (61)$$

$$\frac{\partial T_{\text{slide}}}{\partial \mathbf{u}_\ell^e} = -\frac{\mu_{\text{EA}}}{J_{\text{cl}}^e} T'_n(g_n) \mathbf{N}_\ell^T \mathbf{n}_p - \frac{T_{\text{slide}}}{J_{\text{cl}}^e} \frac{\partial J_{\text{cl}}^e}{\partial \mathbf{u}_\ell^e}. \quad (62)$$

The surface stretch  $J_{\text{cl}}^e$  and its derivatives are given in Eqs. (10) and (44) and

$$\left[ \frac{\partial J_{\text{cl}}^e}{\partial \mathbf{u}_\ell^e} \right]^T = -J_{\text{cl},\alpha}^e c_p^{\alpha\beta} [\mathbf{a}_\beta^p]^T \mathbf{N}_\ell(\boldsymbol{\xi}_p) + \left[ J_{\text{cl}}^e \mathbf{a}_p^\beta + g_n J_{\text{cl},\alpha}^e c_p^{\alpha\beta} \mathbf{n}_p \right]^T \mathbf{N}_{\ell,\beta}(\boldsymbol{\xi}_p). \quad (63)$$

## Acknowledgements

This work was initially supported by the German Research Foundation (DFG) under grants SA1822/5-1 and GSC111. JS acknowledges support from the Institut Carnot Ingénierie @ Lyon and from LABEX MANUTECH-SISE (ANR-10-LABX-0075) of the Université de Lyon, within the program “Investissements d’Avenir” (ANR-11-IDEX-0007) operated by the French National Research Agency (ANR). We further thank Dr. Thang X. Duong (RWTH Aachen University) for helpful comments.



## References

- Autumn, K., Sitti, M., Liang, Y. A., Peattie, A. M., Hansen, W. R., Sponberg, S., Kenny, T. W., Fearing, R., Israelachvili, J. N., and Full, R. J. (2002). Evidence for van der Waals adhesion in gecko setae. *Proc. Natl. Acad. Sci. U.S.A.*, **99**(19):12252–12256.
- Berman, A., Drummond, C., and Israelachvili, J. (1998). Amontons’ law at the molecular level. *Tribol. Lett.*, **4**:95–101.
- Bonet, J. and Wood, R. D. (1997). *Nonlinear Continuum Mechanics for Finite Element Analysis*. Cambridge University Press.
- Briscoe, B. J. and Kremnitzer, S. L. (1979). A study of the friction and adhesion of polyethylene-terephthalate monofilaments. *J. Phys. D: Appl. Phys.*, **12**:505–517.
- Chaboche, J. L., Feyel, F., and Monerie, Y. (2001). Interface debonding models: a viscous regularization with a limited rate dependency. *Int. J. Solids Struct.*, **38**:3127–3160.
- Chaboche, J. L., Girard, R., and Schaff, A. (1997). Numerical analysis of composite systems by using inter-phase/interface models. *Comput. Mech.*, **20**:3–11.
- Chen, S., Yan, C., and Soh, A. (2008). Non-slipping JKR model for transversely isotropic materials. *Int. J. Solids Struct.*, **45**:676–687.
- Cohen, C., Restagno, F., Poulard, C., and Léger, L. (2011). Incidence of the molecular organization on friction at soft polymer interfaces. *Soft Matter*, **7**:8535–8541.
- Corbett, C. J. and Sauer, R. A. (2014). NURBS-enriched contact finite elements. *Comput. Methods Appl. Mech. Eng.*, **275**:55–75.
- Corbett, C. J. and Sauer, R. A. (2015). Three-dimensional isogeometrically enriched finite elements for frictional contact and mixed-mode debonding. *Comput. Methods Appl. Mech. Eng.*, **284**:781–806.
- De Lorenzis, L., Temizer, İ., Wriggers, P., and Zavarise, G. (2011). A large deformation frictional contact formulation using NURBS-based isogeometric analysis. *Int. J. Numer. Methods Eng.*, **87**(13):1278–1300.
- De Zotti, V., Rapina, K., Cortet, P.-P., Vanel, L., and Santucci, S. (2019). Bending to kinetic energy transfer in adhesive peel front microinstability. *Phys. Rev. Lett.*, **122**:068005.
- Del Piero, G. and Raous, M. (2010). A unified model for adhesive interfaces with damage, viscosity, and friction. *Eur. J. Mech. A/Solids*, **29**:496–507.
- Deng, Z., Smolyanitsky, A., Li, Q., Feng, X.-Q., and Cannara, R. J. (2012). Adhesion-dependent negative friction coefficient on chemically modified graphite at the nanoscale. *Nat. Mater.*, **11**:1032–1037.
- Derjaguin, B. (1934). Molekulartheorie der äußeren Reibung. *Z. Phys.*, **88**:661–675.
- Dittmann, M., Franke, M., Temizer, İ., and Hesch, C. (2014). Isogeometric analysis and thermomechanical mortar contact problems. *Comput. Methods Appl. Mech. Eng.*, **274**:192–212.
- Eason, E. V., Hawkes, E. W., Windheim, M., Christensen, D. L., Libby, T., and Cutkosky, M. R. (2015). Stress distribution and contact area measurements of a gecko toe using a high-resolution tactile sensor. *Bioinspir. Biomim.*, **10**:016013.
- Gao, J., Luedtke, W. D., Gourdon, D., Ruths, M., Israelachvili, J. N., and Landman, U. (2004). Frictional forces and Amontons’ law: From the molecular to the macroscopic scale. *J. Phys. Chem. B*, **108**:3410–3425.
- Gitterle, M., Popp, A., Gee, M. W., and Wall, W. A. (2010). Finite deformation frictional mortar contact using a semi-smooth Newton method with consistent linearization. *Int. J. Numer. Methods Eng.*, **84**(5):543–571.
- Gouravaraju, S., Sauer, R. A., and Gautam, S. S. (2019). Investigating the normal and tangential peeling behavior of gecko spatulae using a coupled adhesion-friction model. arXiv preprint (arXiv:1901.11505).
- Hill, G. C., Soto, D. R., Peattie, A. M., Full, R. J., and Kenny, T. W. (2011). Orientation angle and the adhesion of single gecko setae. *J. R. Soc. Interface*, **8**:926–933.

- Homola, A. M., Israelachvili, J. N., McGuiggan, P. M., and Gee, M. L. (1990). Fundamental experimental studies in tribology: The transition from “interfacial” friction of undamaged molecularly smooth surfaces to “normal” friction with wear. *Wear*, **136**:65–83.
- Jagota, A. and Hui, C.-Y. (2011). Adhesion, friction, and compliance of bio-mimetic and bio-inspired structured interfaces. *Mater. Sci. Eng. R*, **72**:253–292.
- Johansson, L. and Klarbring, A. (1993). Thermoelastic frictional contact problems: Modelling, finite element approximation and numerical realization. *Comput. Methods Appl. Mech. Eng.*, **105**(2):181–210.
- Khajeh Salehani, M., Irani, N., and Nicola, L. (2019). Modeling adhesive contacts under mixed-mode loading. *J. Mech. Phys. Solids*, **130**:320–329.
- Krstulović-Opara, L., Wriggers, P., and Korelc, J. (2002). A  $C^1$ -continuous formulation for 3D finite deformation frictional contact. *Comput. Mech.*, **29**(1):27–42.
- Labonte, D., Williams, J. A., and Federle, W. (2014). Surface contact and design of fibrillar ‘friction pads’ in stick insects (*Carausius morosus*): mechanisms for large friction coefficients and negligible adhesion. *J. R. Soc. Interface*, **11**:20140034.
- Laursen, T. A. (2002). *Computational Contact and Impact Mechanics*. Springer.
- Laursen, T. A. and Simo, J. C. (1993). A continuum-based finite element formulation for the implicit solution of multibody, large deformation-frictional contact problems. *Int. J. Numer. Methods Eng.*, **36**:3451–3485.
- Martins, J. A. C. and Raous, M., editors (2002). *Friction and Instabilities*, volume 457 of *CISM International Centre for Mechanical Sciences Courses and Lectures*. Springer, Wien.
- Mergel, J. C. (2017). *Advanced Computational Models for the Analysis of Adhesive Friction*. Doctoral thesis, RWTH Aachen University, Germany.
- Mergel, J. C., Sahli, R., Scheibert, J., and Sauer, R. A. (2019). Continuum contact models for coupled adhesion and friction. *J. Adhesion*, **95**(12):1101–1133.
- Mo, Y., Turner, K. T., and Szlufarska, I. (2009). Friction laws at the nanoscale. *Nature*, **457**:1116–1119.
- Mróz, Z. (2002). Contact friction models and stability problems. In Martins, J. A. C. and Raous, M., editors, *Friction and Instabilities*, volume 457 of *CISM International Centre for Mechanical Sciences Courses and Lectures*, pages 179–232. Springer, Wien.
- Padmanabhan, V. and Laursen, T. A. (2001). A framework for development of surface smoothing procedures in large deformation frictional contact analysis. *Finite Elem. Anal. Des.*, **37**(3):173–198.
- Papangelo, A. and Ciavarella, M. (2019). On mixed-mode fracture mechanics models for contact area reduction under shear load in soft materials. *J. Mech. Phys. Solids*, **124**:159–171.
- Papangelo, A., Scheibert, J., Sahli, R., Pallares, G., and Ciavarella, M. (2019). Shear-induced contact area anisotropy explained by a fracture mechanics model. *Phys. Rev. E*, **99**:053005.
- Ponce, S., Bico, J., and Roman, B. (2015). Effect of friction on the peeling test at zero-degrees. *Soft Matter*, **11**:9281–9290.
- Puso, M. A. and Laursen, T. A. (2004). A mortar segment-to-segment frictional contact method for large deformations. *Comput. Methods Appl. Mech. Eng.*, **193**(45–47):4891–4913.
- Raous, M. (2011). Interface models coupling adhesion and friction. *C. R. Méc.*, **339**:491–501.
- Raous, M., Cangémi, L., and Cocu, M. (1999). A consistent model coupling adhesion, friction, and unilateral contact. *Comput. Methods Appl. Mech. Eng.*, **177**:383–399.
- Ruths, M., Berman, A. D., and Israelachvili, J. N. (2005). Surface forces and nanorheology of molecularly thin films. In Bhushan, B., editor, *Nanotribology and Nanomechanics*, pages 389–481. Springer, Berlin Heidelberg.
- Sahli, R., Pallares, G., Ducottet, C., Ben Ali, I. E., Al Akhrass, S., Guibert, M., and Scheibert, J. (2018). Evolution of real contact area under shear and the value of static friction of soft materials. *Proc. Natl. Acad. Sci. U.S.A.*, **115**(3):471–476.

- Sahli, R., Pallares, G., Papangelo, A., Ciavarella, M., Ducottet, C., Ponthus, N., and Scheibert, J. (2019). Shear-induced anisotropy in rough elastomer contact. *Phys. Rev. Lett.*, **122**:214301.
- Sauer, R. A. (2006). *An Atomic Interaction based Continuum Model for Computational Multiscale Contact Mechanics*. PhD thesis, University of California, Berkeley, USA.
- Sauer, R. A. (2011). Enriched contact finite elements for stable peeling computations. *Int. J. Numer. Methods Eng.*, **87**:593–616.
- Sauer, R. A. and De Lorenzis, L. (2013). A computational contact formulation based on surface potentials. *Comput. Methods Appl. Mech. Eng.*, **253**:369–395.
- Sauer, R. A. and De Lorenzis, L. (2015). An unbiased computational contact formulation for 3D friction. *Int. J. Numer. Methods Eng.*, **101**(4):251–280.
- Sauer, R. A., Duong, T. X., and Corbett, C. J. (2014). A computational formulation for constrained solid and liquid membranes considering isogeometric finite elements. *Comput. Methods Appl. Mech. Eng.*, **271**:48–68.
- Sauer, R. A. and Li, S. (2007a). An atomic interaction-based continuum model for adhesive contact mechanics. *Finite Elem. Anal. Des.*, **43**(5):384–396.
- Sauer, R. A. and Li, S. (2007b). A contact mechanics model for quasi-continua. *Int. J. Numer. Methods Eng.*, **71**:931–962.
- Sauer, R. A. and Mergel, J. C. (2014). A geometrically exact finite beam element formulation for thin film adhesion and debonding. *Finite Elem. Anal. Des.*, **86**:120–135.
- Sauer, R. A. and Wriggers, P. (2009). Formulation and analysis of a three-dimensional finite element implementation for adhesive contact at the nanoscale. *Comput. Methods Appl. Mech. Eng.*, **198**:3871–3883.
- Simo, J. C. and Hughes, T. J. R. (1998). *Computational Inelasticity*. Springer.
- Sivebæk, I. M., Samoilov, V. N., and Persson, B. N. J. (2008). Frictional properties of confined polymers. *Eur. Phys. J. E*, **27**:37–46.
- Strömberg, N., Johansson, L., and Klarbring, A. (1996). Derivation and analysis of a generalized standard model for contact, friction and wear. *Int. J. Solids Struct.*, **33**(13):1817–1836.
- Tabor, D. (1981). Friction — the present state of our understanding. *J. Lubr. Technol.*, **103**:169–179.
- Temizer, İ., Wriggers, P., and Hughes, T. J. R. (2012). Three-dimensional mortar-based frictional contact treatment in isogeometric analysis with NURBS. *Comput. Methods Appl. Mech. Eng.*, **209–212**:115–128.
- tribonet.org (2019). <https://www.tribonet.org/should-the-contact-area-really-increase-due-to-sliding-and-why-this-is-never-observed/> (accessed on 27 December, 2019).
- Vakis, A. I., Yastrebov, V. A., Scheibert, J., Nicola, L., Dini, D., Minfray, C., Almqvist, A., Paggi, M., Lee, S., Limbert, G., Molinari, J. F., Anciaux, G., Aghababaei, R., Echeverri Restrepo, S., Papangelo, A., Cammarata, A., Nicolini, P., Putignano, C., Carbone, G., Stupkiewicz, S., Lengiewicz, J., Costagliola, G., Bosia, F., Guarino, R., Pugno, N. M., Müser, M. H., and Ciavarella, M. (2018). Modeling and simulation in tribology across scales: An overview. *Tribol. Int.*, **125**:169–199.
- Waters, J. F. and Guduru, P. R. (2010). Mode-mixity-dependent adhesive contact of a sphere on a plane surface. *Proc. R. Soc. A*, **466**:1303–1325.
- Wriggers, P. (2006). *Computational Contact Mechanics*. Springer, Berlin Heidelberg, 2<sup>nd</sup> edition.
- Wriggers, P. (2008). *Nonlinear Finite Element Methods*. Springer, Berlin Heidelberg.
- Wriggers, P. and Krstulović-Opara, L. (2004). The moving friction cone approach for three-dimensional contact simulations. *Int. J. Comput. Methods*, **1**(1):105–119.
- Wriggers, P. and Reinelt, J. (2009). Multi-scale approach for frictional contact of elastomers on rough rigid surfaces. *Comput. Methods Appl. Mech. Eng.*, **198**:1996–2008.
- Wriggers, P., Vu Van, T., and Stein, E. (1990). Finite element formulation of large deformation impact-contact problems with friction. *Comput. Struct.*, **37**(3):319–331.

Zeng, H., Pesika, N., Tian, Y., Zhao, B., Chen, Y., Tirrell, M., Turner, K. L., and Israelachvili, J. N. (2009). Frictional adhesion of patterned surfaces and implications for gecko and biomimetic systems. *Langmuir*, **25**(13):7486–7495.